ABSTRACT

Title of Thesis: AEROACOUSTIC ANALYSIS OF
ASYMMETRIC LIFT-OFFSET
HELICOPTER IN FORWARD FLIGHT

Paulo T Arias Juarez
Master of Science in Aerospace Engineering, 2021

Thesis Directed by: Professor James Baeder
A. James Clark School of Engineering
Department of Aerospace Engineering

In recent years, the University of Maryland has worked on an asymmetric lift-offset compound helicopter. The configuration consists of a single main rotor helicopter with the addition of two key ways to increase the forward speed: a stubbed wing on the retreating fuselage side, and a slowed down rotor. Experiments and simulations have shown that the novel concept provides improved thrust potential and lift-to-drag ratios in high-speed forward flight. This study aims to determine whether the asymmetric lift-offset configuration also provides aeroacoustic benefits in forward flight in addition to its aerodynamic advantages. The aerodynamic results from previous computational and experimental studies are recreated using the Mercury framework, in-house Computational Fluid Dynamics solver based on Reynolds-Averaged Navier-Stokes (RANS) coupled to a comprehensive rotor analysis for structural deformations and trim. The acoustic analysis is performed using an acoustic code based on the Ffowcs William-Hawkings equation to solve for the

tonal noise propagating from the surfaces of the aircraft. The BPM model is used for broadband noise prediction. It was found that for an advance ratio of 0.5 the wing-lift offset configuration can produce 56.8% more thrust at the same collective angle without any penalties in total noise. When the configurations produce equal thrust it was found that the wing-lift offset case has a 4 dB reduction in maximum overall sound pressure level. At an advance ratio of 0.3 with trim for equivalent thrust between configurations, a 3 dB maximum OASPL reduction was obtained with the inclusion of the wing. The rotor of the wing-lift offset case was also slowed down while maintaining equal thrust to find a 6 dB reduction at an advance ratio of 0.55. Blade flap and lag bending moments near the root were also significantly reduced for the wing-lift offset configuration with equal thrust.

AEROACOUSTIC ANALYSIS OF ASYMMETRIC LIFT-OFFSET HELICOPTER IN FORWARD FLIGHT

by

Paulo T Arias Juarez

Thesis submitted to the Faculty of the Graduate School of the
University of Maryland, College Park in partial fulfillment
of the requirements for the degree of
Master of Science
2021

Advisory Committee:
Dr. James Baeder, Chair/Advisor
Dr. Anubhav Datta
Dr. Inderjit Chopra

Acknowledgments

First and foremost I'd like to thank my advisor, Dr. James Baeder for giving me the opportunity to be a part of his research group. Under his advice and guidance I have been able to tackle problems that are interesting, fun, and challenging to work on, this has helped me develop greatly both as an academic and a professional.

I would like to thank my colleagues at the rotorcraft center for their constant help throughout my degree, as well as previous students in the lab who developed the codes that I extensively used for my work. I would like to particularly thank Yong Su Jung, since he has been there to help and share his knowledge at every step of my research, particularly when setting up and troubleshooting new cases and simulations. Jan Faust performed the research and analysis that were necessary to recreate the asymmetric lift-offset configuration computationally, and provided the necessary advice and data in order to get me started with this topic. Dilhara Jayasundara was constantly involved in further developing the acoustic code utilized, and helped address specific issues related to my cases.

My deepest thanks are to my parents, I would not be where I am without their love and support.

I would like to thank VLRCOE for providing the funding support for my research.

Table of Contents

List of Tables

List of Figures

List of Abbreviations

ACUM	Acoustic Code University of Maryland
BDF2	2nd order Backwards Differentiation
BPF	Blade Passing Frequency
BPM	Brooks-Pope-Marcolini
CFD	Computational Fluid Dynamics
CSD	Computational Structural Dynamics
dB	Decibels
dBA	A-weighted Decibels
DDES	Delayed Detached Eddy Simulation
FFT	Fast Fourier Transform
FW-H	Fowcs Williams-Hawkings
GARFIELD	Graphics Processing Unit Accelerated Rotor Flow Field Solver
GPU	Graphics Processing Unit
HAMSTR	Hamiltonian Strand Solver
Hz	Hertz
LBL	Laminar Bounday Layer
LES	Large Eddy Simulation
OASPL	Overall Average Sound Pressure Level
Pa	Pascals
PRASADUM	Parallelized Rotorcraft Analysis for Simulation and Design
RMS	Root Mean Square
RPM	Revolutions Per Minute
RANS	Reynolds-Averaged Navier-Stokes
SA	Spalart-Allmaras
SS	Separation/Stall
SPL	Sound Pressure Level
TBL	Turbulent Boundary Layer
TE	Trailing Edge
TEB	Trailing Edge Bluntness
TIOGA	Topology Independent Overset Grid Assembler
TVF	Trailing Edge Vortex Formation
VS	Vortex Shedding
VTOL	Vertical Take-off and Landing
WENO	Weighted Essentially Non-Oscillatory

x

Chapter 1: Introduction

1.1 Motivation

Lift-offset helicopter configurations are a growing field of study in the world of rotorcraft. Configurations such as the coaxial, like the Sikorsky X2 (Figure 1.1), and compound helicopters, like the Airbus RACER, are examples of lift-offset rotorcraft which aim to go past the forward flight limitations of the conventional single main rotor helicopter. The basic aim of such configurations is to shift the thrust production of the rotor to its advancing side, and consequently allowing it to follow its natural tendency to produce more thrust on the advancing side than the retreating side. Coaxial helicopters can achieve this because the two rotors rotate in opposite directions and therefore cancel out the rolling moments generated by each other. Compound helicopters can achieve lift-offset by differential flap deflection on the symmetric wings. By definition, a helicopter with lift-offset will have additional lifting components to generate the necessary moment, therefore one of the challenges of studying these configurations lies in understanding the complex aerodynamics that results from the interactions between the increased number of components. Many previous studies have focused on design optimization and flight mechanics of this concept using low-fidelity tools, while more recently, high-fidelity

Figure 1.1: Sikorsky X2 Coaxial Helicopter

aerodynamics/aeroacoustics simulation tools have been utilized for better prediction at a few representative flight conditions [6, 7]. In these previous studies, Computational Fluid Dynamics (CFD) based on Reynolds-Averaged Navier-Stokes (RANS) have been used to predict the complex interactional flows between the components at trimmed conditions after coupling with Computational Structural Dynamics (CSD).

In recent years, the University of Maryland has worked on a similar configuration: an asymmetric lift-offset compound helicopter. The configuration aims to achieve lift-offset with a single stubbed wing located on the retreating side of the fuselage, see Figure 1.2. While wind tunnel tests and computational aerodynamic simulations have been performed for this configuration, the acoustics of the aircraft has not been previously analyzed. The availability of experimental data for validation provides an opportunity for a tool development study that will better establish

the capability for acoustic predictions for rotorcraft using codes developed at the University of Maryland. Some of the trends observed in the cases studied may also give insight into the impact of the wing on acoustic performance of the aircraft despite the rotor having a low rotational tip mach number. The inclusion of a wing for lift-offset purposes has the potential to have an impact on the noise generation of the aircraft. Since the lift-offset is provided by a steady source of lift, it is possible that the rotor noise will decrease, however the location of the wing underneath the rotor may also cause it to generate noise. Understanding the interactional aeroacoustics of this novel aircraft, as well as further developing the tools and methodology for acoustic prediction of the University of Maryland is what motivates this study.

1.2   Background

This section consists of a description of the configuration studied and the sources of noise that will be encountered. The physical mechanisms that cause each noise source and methods for measuring them are also discussed.

1.2.1   Asymmetric Lift-offset Configuration

The configuration consists of a single main rotor helicopter with the addition of two key ways to increase the forward flight speed: a stubbed wing on the retreating fuselage side, and a slowed down rotor. Figure 1.2 shows the asymmetric lift-offset configuration being tested at the Glenn L. Martin wind tunnel. The stubbed wing aids with thrust production and helps counteract the negative rolling moment that

3
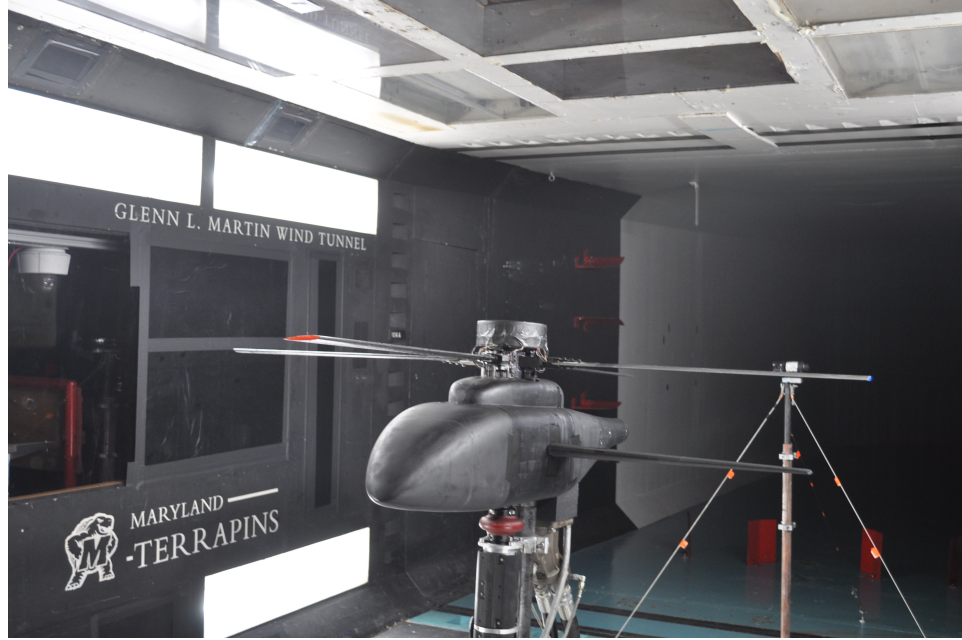
Figure 1.2: Wing-trim case mounted in the Glenn L. Martin Wind Tunnel [4]

arises at high advance ratios. The slowed down rotor helps delay compressibility effects on the advancing side at the expense of an increased advance ratio. Experiments and simulations [1, 4, 5] have shown that the novel concept provides improved thrust and lift-to-drag ratios in high-speed forward flight. Especially, Faust et al. showed improved correlation with experiments using coupled CFD/CSD simulation at advance ratios of 0.3 and 0.5 in terms of trimmed control angles and integrated rotor forces, compared to the results using the low-fidelity comprehensive code [5]. This study aims to investigate whether the aerodynamic benefits that have been associated to the wing lift-offset configuration in fast forward flight also translate into an improved aeroacoustic performance.

Although the original intent of the wing was not necessarily noise reduction, the implementation of a wing reduces the amount of unsteady lift that must be

generated by the main rotor. This could potentially have an impact on the sound levels produced by the configuration, particularly when it comes to loading sound pressure level since it depends on the unsteady aerodynamic forces. A study by Dilhara et al. [17] analyzed the acoustic performance of a wingtip-mounted propeller and found that the wing could produce more noise than the propeller itself, therefore it is not guaranteed that the wing will be quiet for the asymmetric lift-offset configuration. However, the conditions are different for this configuration, the wing is not right next to the rotor and the surface area of the wing is small relative to the rotor. These differences point towards a quieter wing in the asymmetric lift-offset configuration.

The study presented uses the CFD/CSD coupling setup by Faust et al. [5] in order to evaluate the aeroacoustics of the wing lift-offset aircraft. Two configurations are compared throughout the study, one including the wing (wing-trim), and one without the wing (normal-trim). Once the trim conditions with different forward flight speeds and control angles have been achieved for each case, the CFD results can be utilized for acoustic analysis. The unsteady distributed surface pressure of the vehicle is used as an input for the in-house acoustic code of the University of Maryland (ACUM)[3, 16, 17] in order to find loading and thickness overall average sound pressure levels (OASPL). ACUM has been validated for various rotors including forward flight for the SMART rotor[3], HART-II[16], and a wingtip-mounted propeller [17].

The high-fidelity CFD analysis and acoustic analysis based on surface pressure data allows for the individual contributions of each component to be investigated

separately. Isolating the contributions from each component helps explain the effects of the interactional aerodynamics on each part of the configuration, it will also determine which components contribute the most to the total noise. Since two advance ratios are investigated, this study will also be able to determine whether a larger acoustic benefit is achieved at different forward flight speeds.

1.2.2   Loading Noise

Loading noise is one of the two sources of tonal noise and occurs as a result of the unsteady aerodynamic loads that are experienced by the aircraft. These loads will manifest as unsteady pressure variations throughout the surfaces of the helicopter. The maximum loading noise is encountered out of the rotor plane and is represented by dipole sources in the FW-H equations [18]. Because loading noise depends on aerodynamic loads, the accuracy of predictions of this noise source will depend on the accuracy of the aerodynamic simulations. Loading noise is the main source of tonal noise throughout this study, being consistently about 40 dB louder than thickness noise. Any surface of the aircraft which experiences unsteady pressure fluctuations will generate loading noise, therefore even non-rotating parts of the aircraft such as the wing and fuselage will also be a source of loading noise.

1.2.3   Thickness Noise

Thickness noise is the second source of tonal noise and occurs due to the displacement of air by the geometry of the blade as it rotates. Thinner blades that

have a resulting lower volume will have reduced thickness noise than thicker rotating components. Thickness noise will also depend on the rotational speed of the rotating component. This source of noise has a maximum value in the plane of rotation of the rotor and is represented by a monopole source distribution from the surface of the blade. The thickness noise is considerably lower than loading noise throughout this study. The rotor blades are the only components that will generate thickness noise.

1.2.4 Broadband Noise

Also called self-noise, broadband noise occurs due to interactions between an airfoil and its own turbulence produced by its boundary layer and near wake [19]. As suggested by the name, broadband noise occurs over a more broad range of frequencies than the other sources of noise. Broadband noise typically dominates over the other noise sources at higher frequencies. Five different mechanisms for broadband noise generation are identified and predicted in the Brooks-Pope-Marcolini (BPM) method:

(1) Turbulent Boundary Layer-Trailing Edge (TBL-TE) noise

(2) Turbulent Boundary Layer-Separation/Stall (TBL-SS) noise
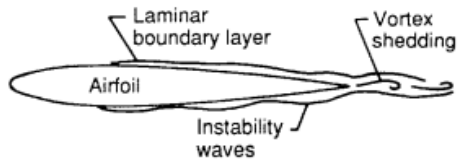
(3) Laminar Boundary Layer-Vortex Shedding (LBL-VS) noise
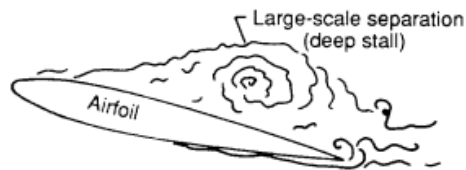
(4) Tip Vortex Formation (TVF) noise
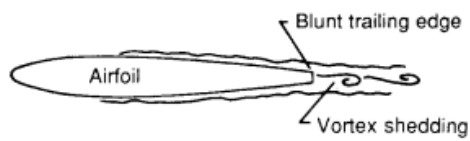
(5) Trailing Edge Bluntness-Vortex Shedding (TEB-VS) noise

A visualization of each mechanism can be seen in Figure 1.3.

1.2.5   Measuring Noise

In this study acoustic results will be reported using three different methods of noise measurement, Sound Pressure Level, Overall Average Sound Pressure Level, and A-weighted decibels.

(1) Sound Pressure Level (SPL): This is the most common method for measuring noise. SPL is in units of decibels (dB) and represents a comparison between pressure fluctuations over a period of time and a reference pressure. Equation 1.1 shows how the calculation of SPL is expressed mathematically.

$$dB = 20log_{10}\left(\frac{p}{p_{ref}}\right) \tag{1.1}$$

The variable p is the pressure fluctuation from ambient pressure, these fluctuations can be found over a period of time by calculating the root mean squared (RMS) of the values. The reference pressure, p_{ref}, is the lowest pressure difference that the human ear is capable of hearing, that is, 20 μPa. The base ten logarithm of the ratio of these pressures is then calculated to account for the large changes in pressure fluctuation necessary to increase noise generation. Figure 1.4 shows how loud a human perceives decibels, keep in mind that human perception will also dependent on the frequency at which the noise is produced.

Figure 1.3: Flow conditions producing airfoil blade self-noise. [19]
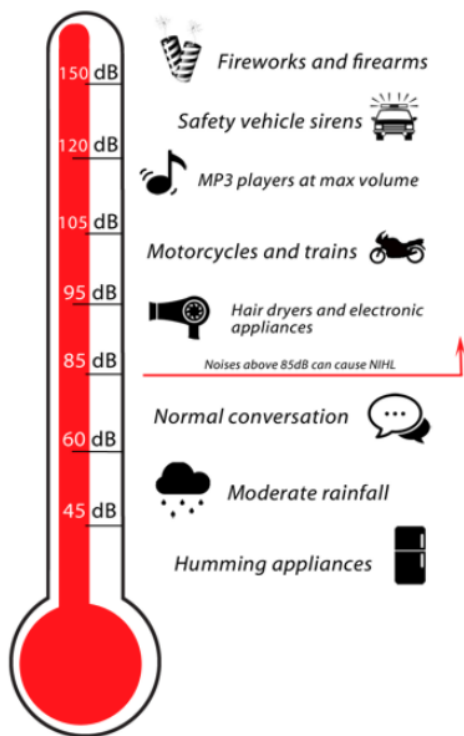
Figure 1.4: Common sounds in terms of decibels

(2) Overall Average Sound Pressure Level (OASPL): While SPL represents sound at a specific frequency, OASPL combines all the frequencies to report the overall noise that is coming from a source. A Fast Fourier Transform (FFT) is utilized to find the specific decibel values at each frequency, once the values are calculated, they are integrated across the spectrum to find the corresponding OASPL. OASPL is often used to report the noise generated by a source in a more concise manner, it is also measured in units of decibels.

(3) A-Weighted Decibels (dBA): As mentioned in the discussion about SPL, different frequencies are perceived differently by the human ear. A-weighting is a way to account for the dependence on frequency of noise perception. Figure 1.5 shows how A-weighting would affect a 60 dB SPL signal at different frequencies. Note that the weighting is such that frequencies below 1000 Hz and above 6000 Hz are attenuated, while frequencies in between these values are slightly enhanced.

1.3   Thesis Contributions

The recent studies on the asymmetric lift-offset configuration aim to increase our knowledge about this type of aircraft. The research on this topic allow us to quantify the potential benefits and drawbacks of such a helicopter. Increased knowledge of the configuration may in time show that it is an aircraft worth developing for production. Even if the configuration does not end up being produced, the isolated benefits discovered from the analysis may aid in the improvement and development

11
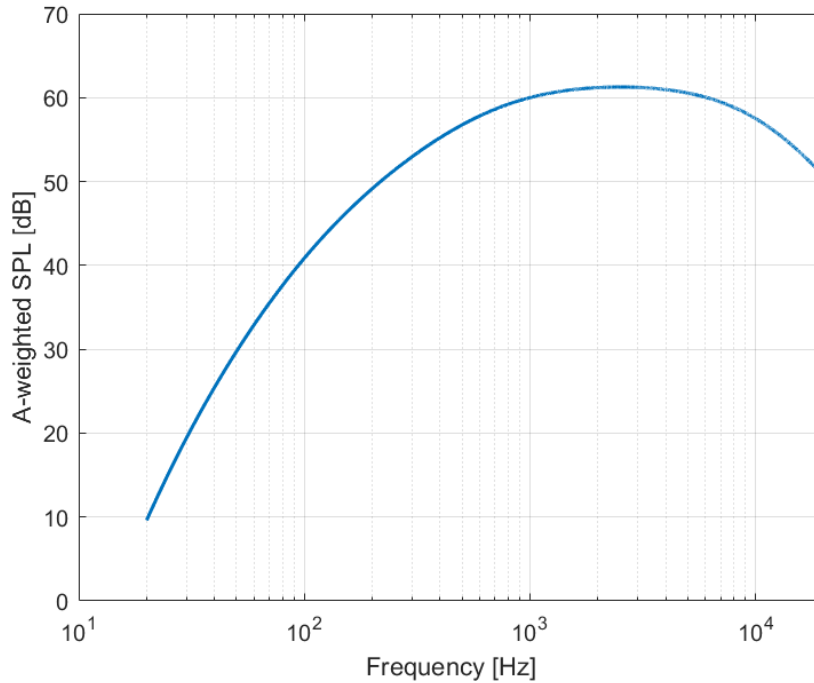
Figure 1.5: 60 dB SPL signals of different frequencies subjected to A-weighting

of other aircraft. This thesis contributes to the body of knowledge of the asymmetric lift-offset configuration by identifying the potential aerodynamic, aeroacoustic, and vibratory benefits of the aircraft with high-fidelity methods.

Most studies of rotorcraft acoustics limit their analysis to the rotating components of the aircraft, as a result, there is limited information on the noise generation of non-rotating components. The present study is able to analyze the non-rotating components of the aircraft just as well as the rotor due to ACUM's ability to directly use surface pressure data information as a source of noise. Other methods which use compact chord approximations are limited to only rotor noise estimations and are less accurate.

The acoustic analysis provided for the configuration is thorough. The acoustics

for all the components of the helicopter are analyzed accounting for the interactions between them. An analysis of the frequencies at which noise is produced is also performed, this allows us to also perform an A-weighting of the acoustic results for each component of each case. Finally, Appendix A also includes a study of the broadband noise using the BPM method.

This thesis provides results for different trim conditions than those previously studied. In previous experimental and computational research, the trim objectives for the cases studied were limited to achieving zero rolling and pitching moment at a fixed collective angle. These methods were more appropriate in a wind tunnel test setting since it allows us to determine the differences in thrust production between a rotor of a configuration with the asymmetric wing and without it. However, for a fair comparison between a configuration with and without the wing, it is essential that the two aircraft are producing equivalent total thrust. This study performs trims for equivalent thrust and compares them to the previous cases analyzed in order to better understand the benefits of the configuration under a fair comparison. In this thesis a further reduced RPM for the case with a wing is also investigated as a way to find the most acoustically beneficial trim state.

1.4   Outline of Thesis

In this thesis an aerodynamic analysis will be performed for a set of differently trimmed aircraft in order to investigate the benefits of the asymmetric lift-offset configuration. The aerodynamic results will be used to perform an in depth inter-

actional aeroacoustic analysis of the configurations to also find potential acoustic benefits. The multiple trim conditions analyzed will allow to identify the most beneficial flight conditions for the aircraft in terms of noise generation. From this point the thesis will proceed as follows:

- Chapter 2: The methodology for the aerodynamic, structural, and aeroacoustic analysis is described in detail. The process of obtaining the acoustic results is followed, including the CFD framework, the CFD/CSD coupling required to obtain the trimmed configurations, and the acoustic framework. This chapter includes in-depth information about the experimental and computational setup, as well as detailed characteristics of the aircraft itself.

- Chapter 3: The aerodynamic results for all the cases with different advance ratios and trim objectives. This chapter includes a the convergence of the CFD/CSD coupling process and different visualizations of the aerodynamic results that may allow for connections to their expected acoustic impact.

- Chapter 4: The aeroacoustic results for all the cases analyzed. This chapter will show the acoustic results for every component of every case and comparisons between them. Additionally, effects from the wind tunnel on the asymmetric lift-offset configuration acoustic analysis are discussed in this chapter.

- Chapter 5: An analysis of the vibratory loads for the rotors of each of the cases. This chapter takes advantage of the information available from the comprehensive code to investigate the predicted vibratory loads caused by lag and flap bending moments.

- Chapter 6: A summary of all results is presented in this chapter. Conclusions are drawn from this results about the potential of the asymmetric lift-offset configuration. Possible future work is also discussed.

- Appendix A: Broadband noise results are presented. The appendix analyzes the broadband noise results and explains why these were not integrated with the rest of the acoustic results. A thought experiment is presented to describe a different study in which broadband noise analysis is more appropriate.

Chapter 2: Methodology

2.1 Overview

The methodology utilized in this thesis to calculate the acoustic results for the asymmetric lift-offset configuration depends on three main codes or frameworks. The first is a comprehensive code which computes an initial guess for the aerodynamic and structural loads in order to predict the control angles necessary for trimmed flight. The comprehensive code is then corrected with CFD simulations in a process called CFD/CSD delta coupling, this will be further explained in section 2.2.3. Once the aircraft is trimmed, the surface pressure data from the CFD results is exported to an acoustic code. The acoustic code then predicts the noise propagation to a set of observers.

2.2 Aerodynamic and Structural Simulations

2.2.1 Comprehensive Code

The structural and low fidelity aerodynamic analysis is done using the Parallelized Rotorcraft Analysis for Simulation and Design (PRASADUM) [14] comprehensive analysis. PRASADUM consists of a Euler-Bernoulli beam structural model

with a lifting line aerodynamic model. The aerodynamic model utilizes 2-D airfoil lookup tables and the Maryland Free Wake model [15]. PRASADUM develops the first approximation of the trim and proceeds to adjust it using the information from the CFD simulation results. Every coupling step PRASADUM calculates the adjusted aerodynamic loads at a set of 20 span-wise locations and 98 azimuthal locations, these loads are used to generate the deflections of the blades based on the loads. PRASADUM also provides predictions of the vibratory loads generated, this functionality will be used in chapter 5 to analyze the vibrations of the cases.

2.2.2   CFD Solvers

The CFD analysis is based on Reynolds-Averaged Navier-Stokes (RANS) and performed using the Mercury framework [8]. This framework is a multi-mesh multi-solver which uses the Graphics Processing Unit Accelerated Rotor Flow Field Solver (GARFIELD) [9] and Hamiltonian Strand solver (HAMSTR) [10] in order to solve discretized overset grid systems.

HAMSTR solves the near body domain by identifying line-structures in unstructured grids, allowing it to perform higher-order stencil-based reconstruction and line-implicit procedures to improve computational efficiency. In the mesh generation process, HAMSTR subdivides an initial grid into quadrilateral cells in order to form loops for line identification. The initial grid can be structured or unstructured. HAMSTR then uses strand volume grid to discretize the domain.

GARFIELD is used to solve the off-body domains as it can only handle struc-

tured grids. GARFIELD, which is also a parallelized code, runs entirely on the GPU. The two solvers communicate within a Python framework. Topology Independent Overset Grid Assembler (TIOGA) [13] is used for connectivity and data interpolation along the overset boundaries between the domains.

The CFD was performed using 5th order Weighted Essentially Non-Oscillatory (WENO) spatial reconstruction for inviscid flux computation, 2nd order central differencing for viscous flux computation, and 2nd Backward Differentiation Formula (BDF2) for implicit time marching. For the turbulence closure, hybrid RANS-LES formulation using one-equation Spalart-Allmaras turbulence model (SA-DDES) is applied. [12] The boundary layer transition is predicted using Medida-Baeder transition model [11] at the measured free-stream turbulence intensity of 0.21% from the wind tunnel facility.

2.2.3 CFD/CSD Coupling

As mentioned, a comprehensive code is first used to perform low-fidelity analysis of the aerodynamic and structural loads on the aircraft. The comprehensive code couples its own structural and aerodynamic codes in order to attempt to find the appropriate control angles to achieve the desired trim objectives. In the process of achieving trim, the comprehensive code will generate a file describing the deformations of the blades in response to the chosen control angles and aerodynamic loads for a full rotor revolution. These blade deformations are utilized in a CFD framework to perform a high-fidelity estimation of the airloads. The CFD airloads
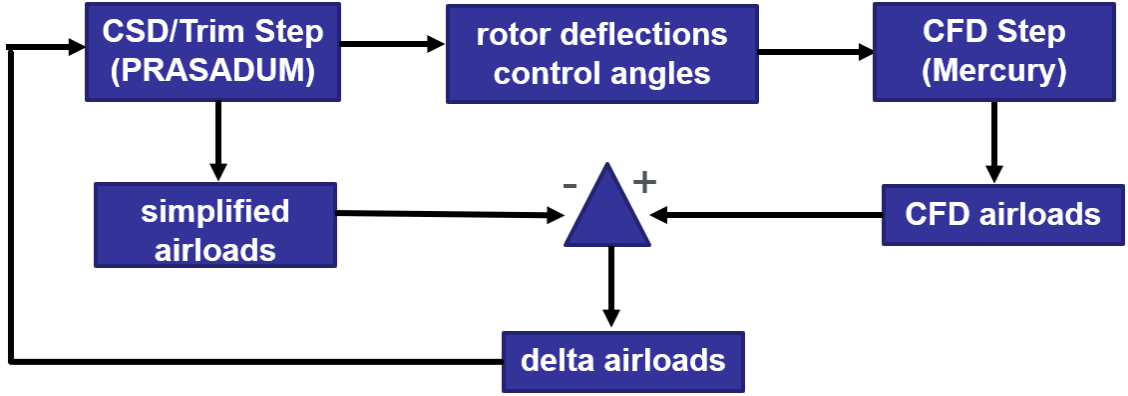
Figure 2.1: CFD/CSD Delta coupling flow diagram

are then accounted for in the comprehensive code to generate new, more accurate blade deflections. This process is referred to as loose delta coupling and is described by Equation 2.1, the method is used and validated in Faust et al. [5]

$$
\begin{aligned}
(F, M)^n_{CSD} &= (F, M)^n_{Caero} + ((F, M)^{n-1}_{Caero} - (F, M)^{n-1}_{CFD}) \\
&= (F, M)^n_{Caero} + \Delta(F, M)^{n-1}
\end{aligned}
\tag{2.1}
$$

Loose delta coupling refers to comparing the CFD and comprehensive code aerodynamic forces and moments (F and M in Equation 2.1) once every revolution, while tight coupling compares the airloads at every time step. Tight delta coupling was not utilized because it requires extensive modifications to the codes and has previously shown to have issues achieving trim. A diagram of the process described for the CFD/CSD coupling can be seen in Figure 2.1. This process is repeated until the trim objectives are achieved in the CFD results within 3% error.
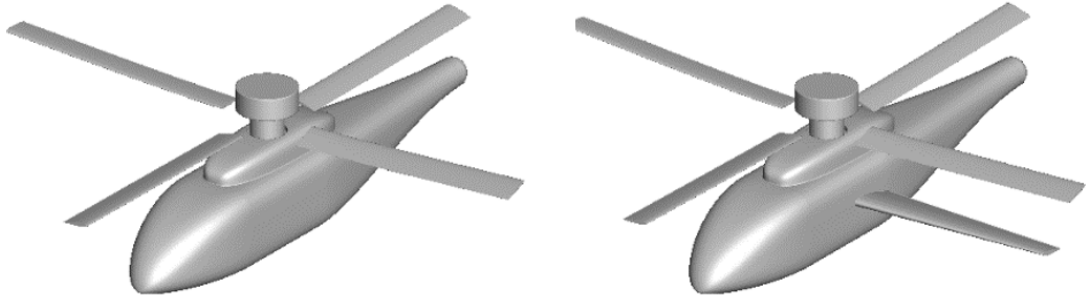
Figure 2.2: Two configurations compared throughout this study: Normal-trim (left) and Wing-trim (right)

2.2.4 Trim Conditions

The previous experimental and computational studies performed for the asymmetric lift-offset configuration had a fixed pitch collective angle of 10.6° as a semi-prescribed trim method for all cases studied. With the collective angle set, the vehicles were trimmed to generate zero pitching and rolling moments at different advance ratios. This was the trim method used in the experiment due to the difficulty in using a conventional trim for target thrust at high advance ratios [1]. For each advance ratio a configuration with and without a wing was studied in order to understand the benefits of the wing on rotor thrust.

In the present study the configuration without a wing and with a fixed collective angle is used as a base case for comparison at the advance ratios of 0.3 and 0.5. Several trims are then performed for the helicopter with an asymmetric wing, mostly aiming to achieve equivalent thrust to that of the case without a wing in order to have a fair comparison. For convenience, throughout this thesis the two configurations studied will be referred to as:

- Normal-trim: Helicopter without the incorporation of a wing.

- Wing-trim: Same aircraft with the addition of a stubbed wing on the retreating side.

The computational models of the normal-trim and wing-trim configurations can be seen in Figure 2.2. There are also two different objectives set when trimming the aircraft, target θ_0 and target C_T. In total there are five different combinations of configuration, trim target, and advance ratio (μ) investigated in this study:

- Normal-trim with target θ_0 at $\mu = 0.5$

- Wing-trim with target θ_0 at $\mu = 0.5$

- Wing-trim with target C_T at $\mu = 0.5$

- Wing-trim with target C_T and 90% RPM at $\mu = 0.55$

- Normal-trim with target θ_0 at $\mu = 0.3$

- Wing-trim with target C_T at $\mu = 0.3$

Note that most of the trims investigated are at an advance ratio of 0.5 since this is the flight condition at which most advantages were found in previous studies. Additionally there are two trim conditions at a 0.3 advance ratio in order to understand the effect of flight speed on noise generation. The wing-trim case with reduced RPM has a higher advance ratio but the same forward flight velocity of 60.3 knots as the other $\mu = 0.5$ cases. When changing the RPM the forward flight

Surface Monopole:
Models Thickness noise

Volume Quadrupole:
Models Compressibility effects
Difficult to compute

$$\Box^2 = \left(\frac{1}{c^2}\right)\left(\frac{\partial^2}{\partial t^2}\right) - \nabla^2$$

$$c^2\Box^2\rho'(x,t) = -\frac{\partial}{\partial x_i}\left(L_i\delta(f)|\nabla_x f|\right) + \frac{\partial}{\partial t}\left(\rho_0 U_n\delta(f)|\nabla_x f|\right) + \frac{\partial^2 \overline{T_{ij}}}{\partial x_i \partial x_j}$$

Wave operator:
Propagates sound to observers

Surface Dipole:
Models Loading noise
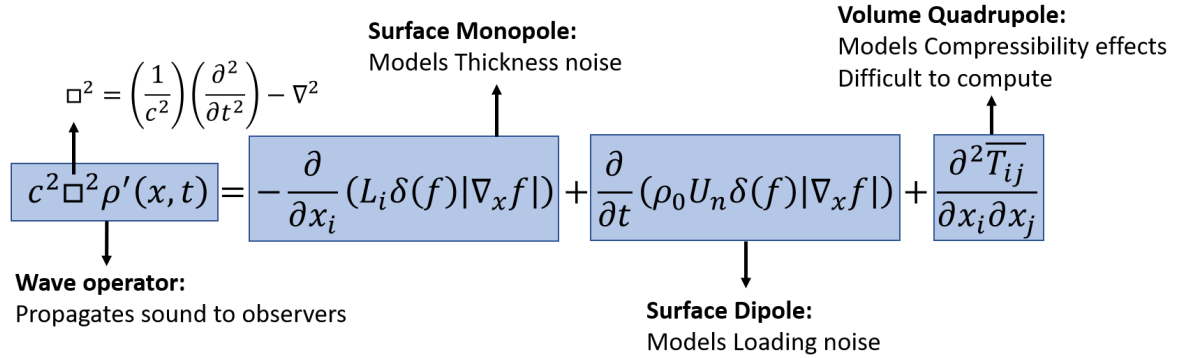
Figure 2.3: Descriptions of terms in Ffowcs Williams-Hawkings Equation

was kept constant instead of μ because this way we can focus on the changes of the rotor noise without changing the mean lift produced by the wing.

2.3 Acoustic Simulations

After the trim objective for a case has been achieved, an additional CFD revolution is conducted in order to ensure that the unsteady solution has converged, and also in order to save the necessary pressure data for the acoustic code. The surface pressure distribution from the final CFD rotor revolution is then fed into ACUM with a 1° azimuthal interval. ACUM stores the pressure data for every surface element in the configuration at all the 360 time steps (one for every degree). The code then uses the Farassat Formulation 1A [18] of the Ffowcs William-Hawkings (FW-H) equation in order to solve for the loading and thickness noise sound pressure level (SPL) that propagates from the surface of the aircraft to a set of observers, the code does not account for broadband noise. Figure 2.3 shows the differential form of the equation used in the code and the significance of each of its terms.
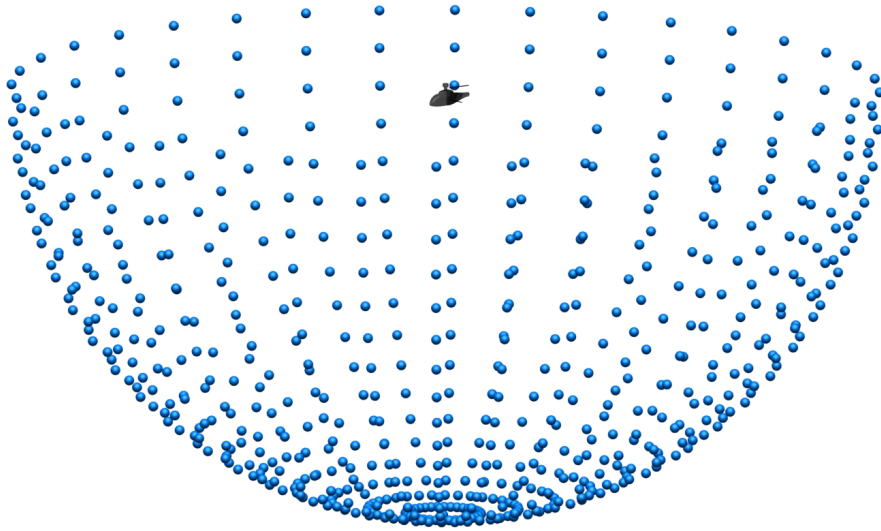
Figure 2.4: 703 acoustic observers located in a hemisphere below the helicopter (helicopter not to scale)

In the case of loading noise, the code will essentially analyze the variations in pressure during the full revolution for each surface element, and then propagate the total noise from each element to all observers. In order to differentiate between the different components of the aircraft, the surface pressure data is split before being given to ACUM. Then each acoustic simulation is performed individually, but it includes the effects on the surface pressure caused by other components in the CFD simulation. There are 703 observers arranged in a hemisphere with a radius of 30 rotor radii placed below the helicopter as seen in Figure 2.4. The SPL at each observer is integrated across all frequencies in order to find the overall sound pressure level (OASPL) around the aircraft.

It was found that the thickness noise does not provide any significant contribution to the total noise of any component of the cases studied, therefore only loading noise will be addressed throughout the study. For comparisons between components

and configurations, the maximum OASPL on the hemisphere will be utilized, this is because the noise generated by each component will propagate differently and the noise distribution on the sphere will vary.

The broadband noise can be computed independently of tonal noise. The BPM method [19] is used for self-noise prediction of the rotor blades. This method requires the inflow velocity, effective angle of attack, zero-lift angle of attack, and trailing edge boundary layer parameters at each section of the blade. The effective angle of attack is extracted from the CFD results by comparing the aerodynamic loads to corresponding airfoil tables generated from 2-D RANS simulations at the appropriate Reynolds number for each section. The boundary layer parameters (δ and δ^*) are determined using empirical curve fits based on NACA0012 data. The broadband noise output is in 1/3 octave spectra and assumes quasi-steady loading. The application of BPM on Mercury CFD data is based on the recent study by Jung et al. [20] Because the tip speed of all cases studied in this thesis is low, broadband noise dominates the noise results with mostly unchanging values between configurations. For this reason, broadband noise results are not included in the acoustic sections of this thesis, and is instead discussed in an independent appendix.

2.4   Simulation Setup

The model consists of a modified ROBIN fuselage with a fixed wing mounted on the retreating side at an 8° incidence angle. The wing was designed to be long and

Rotor Characteristic	English	Metric
Airfoil Profile	NACA 0012	
Rotor Blades, N_b	4	
Root Cutout, R_0	16.4% R	
Rotor Radius, R	33.4 in	0.846 m
Blade Chord, c	3.15 in	0.08 m
Rotor Solidity σ	0.12	
Flap Bending Stiffness EI_y	103.6 lb-ft^2	42.8 N-m^2
Lag Bending Stiffness EI_x	2302.0 lb-ft^2	951.3 N-m^2
Torsional Stiffness, GJ	26 lb-ft^2	7.9 N-m^2
Wing Characteristics	English	Metric
Wing Profile (root,tip)	NACA 0020, 0015	
Wing Span, b_w	23.4 in	0.594 m
Wing Pitch Angle, α_w	8°	
Aspect Ratio, AR	5	
Taper Ratio, λ	0.5	

Table 2.1: Wing Lift-offset Characteristics.[1, 4]
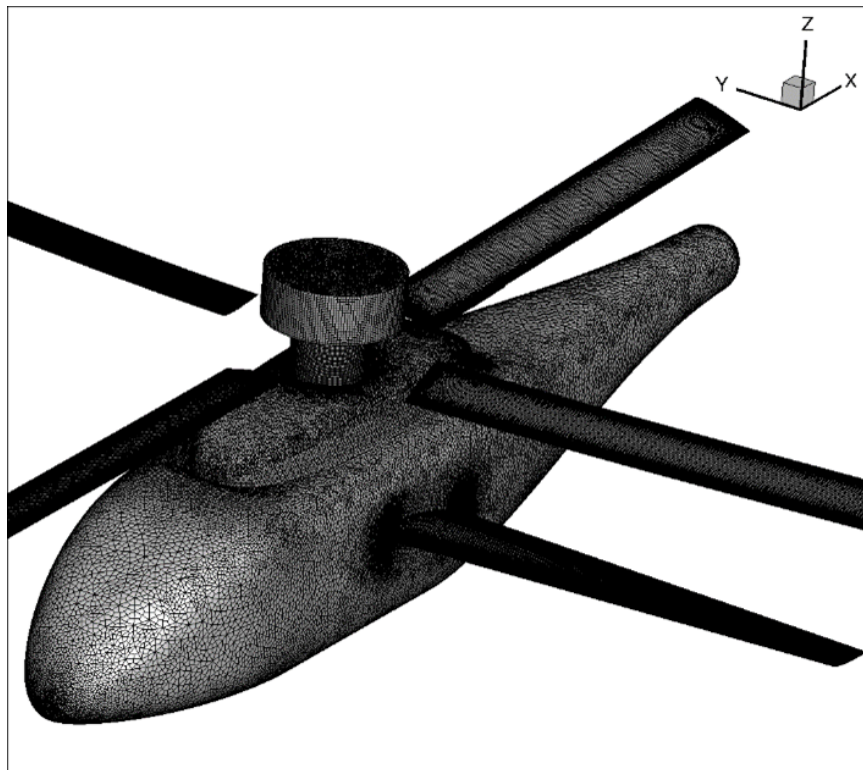
Figure 2.5: Wing-trim case CAD model with surface mesh.

slender in order to maximize its moment generation more than its lift production. The rotor system has 4 unswept and untwisted blades with a NACA 0012 profile. In the experiments, a support is located under the fuselage in order to mount the model in the wind tunnel. The detailed parameters of the blade and wing are as shown in Table 2.1.

Both the normal-trim and wing-trim experimental cases were recreated with CAD models as seen in Figure 2.2. The only differences between the experiment and the CAD are that the hub is simplified and the support structure is removed since it is not necessary in the CFD simulation and was not found to have a significant impact on the aerodynamic results. Figure 2.5 shows the surface mesh on the wing-trim case. Simpler geometries like the hub, blades and wing use a structured mesh, while the fuselage requires an unstructured grid due to its more complicated geometry. The chord-wise and span-wise resolution of the rotor blades and wing surfaces is 224×180 and 208×100 cells respectively. This surface mesh is then used as a starting point to create a strand volume grid using the HAMSTR mesh generator and extensions to the methodology developed by Faust et al. which allows for the volume mesh to be extruded correctly in concave corners in the model. [5]

The near-body mesh is then placed in a set of four nested Cartesian off-body domains of increasing size and coarseness (0.1, 0.25, 0.5, and 2.5 chord lengths) to be solved by GARFIELD, as seen in Figure 2.6. Once the meshes have been created, the rotating motion and deformations prescribed by the comprehensive code are prescribed to the blade domains within the Mercury framework. TIOGA will then communicate the necessary data between cells belonging to different meshes and/or
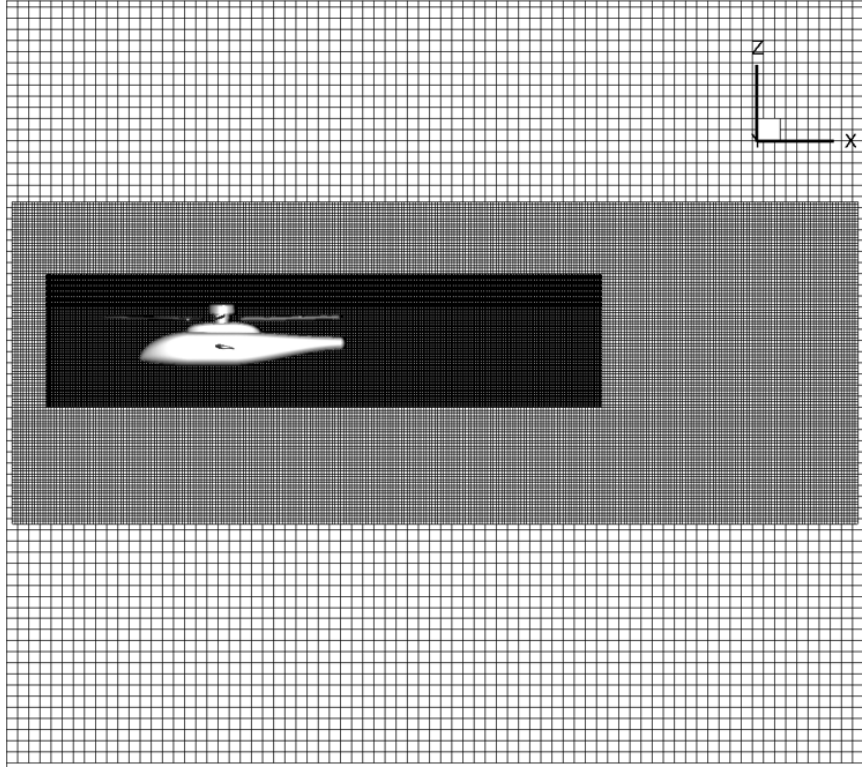
Figure 2.6: Background overset volume mesh.

solvers which are overlapping in space at different time steps. The near-body domain

contains a total of 17.4 million cells, while the background Cartesian grids are made

up of 29.4 million cells. A physical time step equivalent of 0.5° azimuth with 25

sub-iterations is used for the simulations. The wall normal spacing is set to ensure

$y^+ < 1$ for all bodies while targeting a cell load balancing of approximately 140,000-

165,000 cells per CPU.

The rotational speed of the rotor is 700 RPM, the tip mach number is 0.183,

and the tip Reynold's number is 0.338 million. This values are reduced by 10%

only for the reduced RPM trim condition. Free stream Mach numbers of 0.0563 and

0.0911 were used for the 0.3 and 0.5 advance ratio cases respectively. At first, the

CFD simulations were performed using wind tunnel boundary conditions in order

to better match the experimental data, however, it was found that the walls caused acoustic signals which negatively affected results and therefore wind tunnel walls were removed from all simulations in favor of far-field boundary conditions. The effects caused by the wind tunnel walls will be further explained in Section 4.3.

Chapter 3: Aerodynamic Results

This chapter contains the aerodynamic results for all the cases studied visualized in different ways that may aid in making connections to the aeroacoustic results. All the wing-trim cases with different objectives are included and compared to the corresponding normal-trim target θ_0 case at the appropriate advance ratio.

3.1 Full CFD/CSD Coupling

The different cases contained in this chapter were trimmed by using the CFD/CSD coupling and trim objectives described in Sections 2.2.3 and 2.2.4 respectively. Convergence plots of the control angles, thrust, and moment values will be shown in the individual subsections for each case. The results of the coupling process are also summarized in Table 3.1.

From the results of the coupling we can see that the wing-trim target C_T cases have consistently lower control angles than the normal-trim cases at the same advance ratio. This is because the wing produces a substantial amount of thrust at this speeds and therefore off-loads the rotor, detailed information on the thrust production will be shown in the sections for the individual cases. Note that the 90% RPM case has increased control angles when compared to the wing-trim target C_T

	Normal-trim			
Advance ratio, μ	0.3	0.5		
Collective pitch, θ_0	10.6°	10.6°		
Lateral cyclic, θ_{1c}	4.0°	3.1°		
Longitudinal cyclic, θ_{1s}	-7.7°	-10.8°		
Total Thrust Coefficient, C_T	0.0116	0.00830		
	Wing-trim			
Advance ratio, μ	0.3	0.5	0.5	0.55
Trim objective	C_T	θ_0	C_T	C_T 90% RPM
Collective pitch, θ_0	8.7°	10.6°	4.2°	6.0°
Lateral cyclic, θ_{1c}	3.9°	4.4°	3.4°	4.0°
Longitudinal cyclic, θ_{1s}	-5.3°	-9.0°	-2.6°	-4.4°
Total Thrust Coefficient, C_T	0.0114	0.0130	0.00829	0.00834

Table 3.1: Converged control angles and thrust coefficients for each trim condition from CFD/CSD simulations.

case since it is trying to generate the same thrust with a slower rotor.

3.2 Advance Ratio of 0.5

The advance ratio of 0.5 is presented first since it showed the largest advantage for the wing-trim configuration because the wing is able to produce more thrust. Three of the four trim conditions tested for the asymmetric lift-offset configuration are at this advance ratio. The wing-trim target C_T case with reduced RPM is included in this section since it has the same forward flight speed of 60.3 knots, even though it has a higher advance ratio of 0.55.

3.2.1 Target θ_0

The trim for target θ_0 was used in order to stay consistent with previous computational and experimental studies. The convergence of the moments, thrust and control angles for the target θ_0 trim CFD/CSD coupling will not be shown since
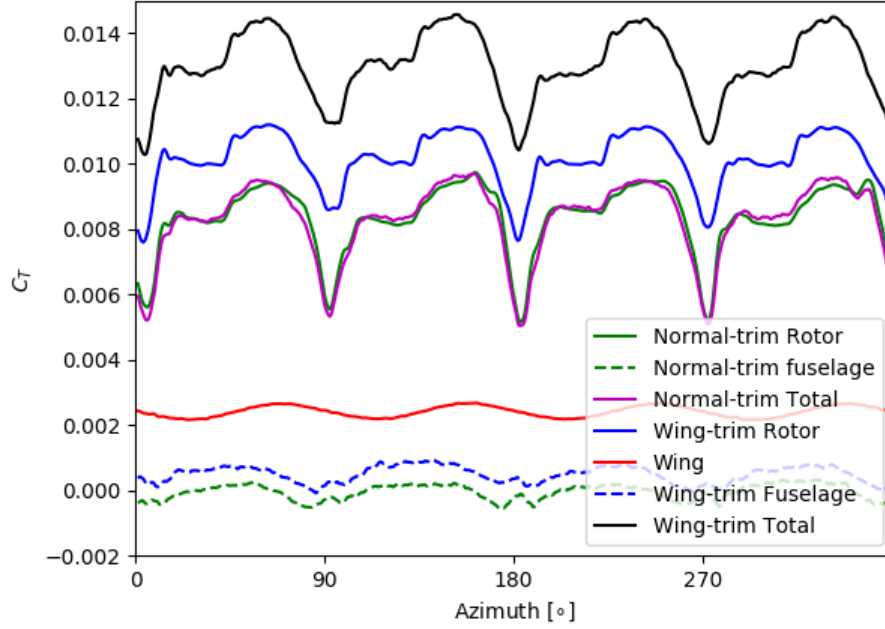
Figure 3.1: Thrust time history of normal-trim and wing-trim cases by component for $\mu = 0.5$ and trimmed for target θ_0.

they can be found in Faust et al. [5], the same deflection files resulting from this study were used in the normal-trim and wing-trim CFD simulations for this section. The resulting control angles for the normal-trim and wing-trim case can be found in Table 3.1. Notice that the wing-trim lateral cyclic is somewhat larger, but the longitudinal cyclic is smaller by a similar difference. The different cyclic angles are a result of the wing changing the moment requirements for the rotor.

The thrust time histories for the components of the normal-trim and wing-trim cases are shown in Figure 3.1. An important first observation from these results is that the wing-trim rotor is capable of producing 21.9% more thrust than the normal-trim rotor due to the help provided by the wing in reducing the negative rolling moment. When the thrust contributions from the rotor, fuselage, and wing are

31

added together, the wing-trim case produces 56.8% more thrust than the normal-trim case. Looking at the other lifting components, the wing alone contributes 18.5% of the total wing-trim case, while the fuselage contributes a smaller 3.7%. It is interesting to note that, while the wing-trim fuselage provides a small contribution to the lift, the normal-trim fuselage produces essentially no lift.

Looking at these results from an acoustic point of view we might think that the wing-trim case will generate more noise since it produces a lot more thrust, however, acoustic analysis is more concerned with the unsteadiness of a source of thrust than its magnitude. Focusing first on the rotor thrust, although the wing-trim rotor generates more thrust, it does so with lower thrust fluctuations on the rotor blades. The larger difference between the cases' total thrust comes mostly from the wing, which is a much steadier source of thrust than the rotors. A way to visualize the possible effects that each component will have on the acoustic results is to plot the root-mean-squared (RMS) of the pressure coefficient fluctuations on the vehicle's surface as seen for the wing-trim case in Figure 3.2. Regions of higher $C_{P_{RMS}}$ and larger surface area will have higher contributions to the total noise of the configuration.

In order to link the aerodynamic results to the acoustics it is helpful to look at the difference in distribution of thrust on the rotor disk between the normal-trim and wing-trim configurations, and more importantly, the distribution of change in thrust with respect to azimuth on the rotor disk for both cases. These plots can be seen in Figure 3.3. The derivative of the thrust with respect to azimuth helps visualize the unsteadiness caused by blade vortex interactions on the advancing side.
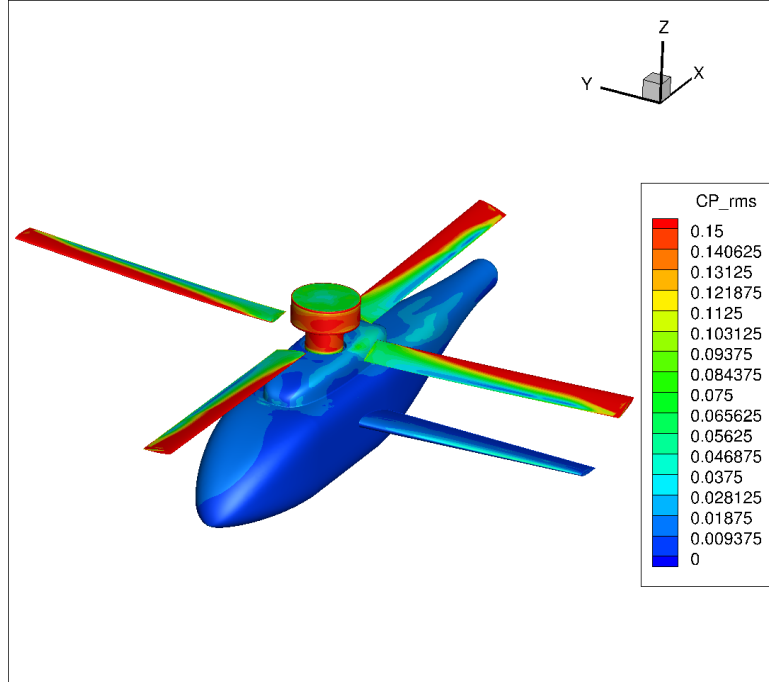
Figure 3.2: Surface pressure coefficient root-mean-squared (RMS) distribution for wing-trim configuration at an advance ratio of 0.5 with trim for target θ_0.

The noise generated due to the BVI's will propagate roughly perpendicular to the span of the blade at the moment the interaction occurs. The regions of unsteady flow are behind the rotor and on the advancing side, which suggests that there will be higher noise in front and to the right of the aircraft. If the normal-trim thrust rotor disc distribution is subtracted from the wing-trim case thrust distribution, the outcome is the left-most contour plot in Figure 3.3. The differences in rotor noise can be further explained by considering this thrust distribution difference, and the comparison between the thrust derivative with respect to azimuth distribution of the cases. It can be seen that the wing-trim case produces more thrust, and that the additional thrust is seen mainly on the advancing side, which is the natural tendency of the rotor in high-speed forward flight. Even though the wing-trim case produces
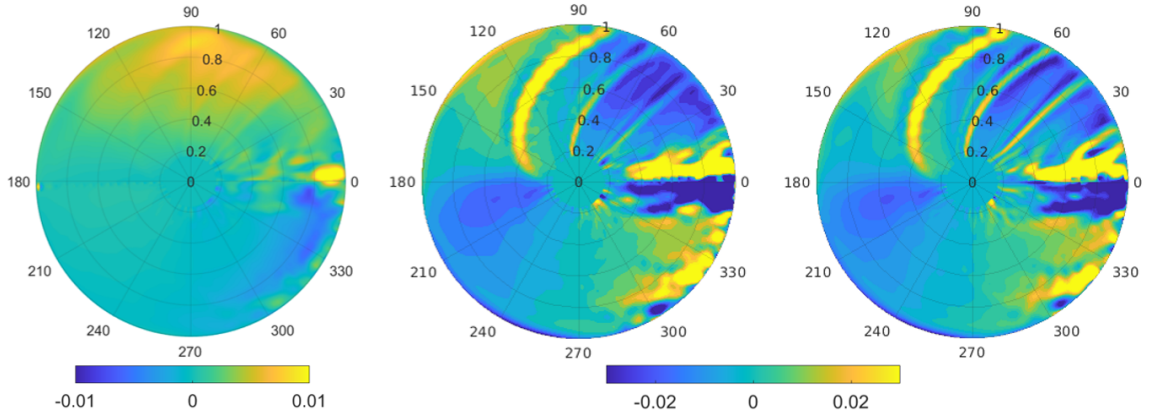
Figure 3.3: Rotor disc contour plots at advance ratio of 0.5: Normal-trim rotor C_N distribution subtracted from Wing-trim rotor C_N with target θ_0 trim. (left) Normal-trim C_N derivative with respect to azimuth. (middle) Wing-trim C_N derivative with respect to azimuth, target θ_0 trim. (last)

more thrust, the time derivative of thrust for both cases is almost identical, which predicts similar noise generation from both rotors.

The source of the large changes in thrust with respect to azimuth in Figure 3.3 can be explained by visualizing the wake structures that form mainly from the blade tips and the hub. A visualization of the wake can be seen in Figure 3.4. The hub leaves a complex wake behind it which the blades have to slice through every revolution, the blade passage through the hub wake causes the large changes in thrust production at the 0° azimuth. The blade vortex interactions can also be seen clearly as the blade in the advancing side has to cut through the tip vortex of the blades ahead of it. The number of BVI encountered depends largely on the advance ratio. Larger advance ratios allow for more dispersion of the tip vortices before a revolution is completed, this will become more evident when looking at the wake in Section 3.3.
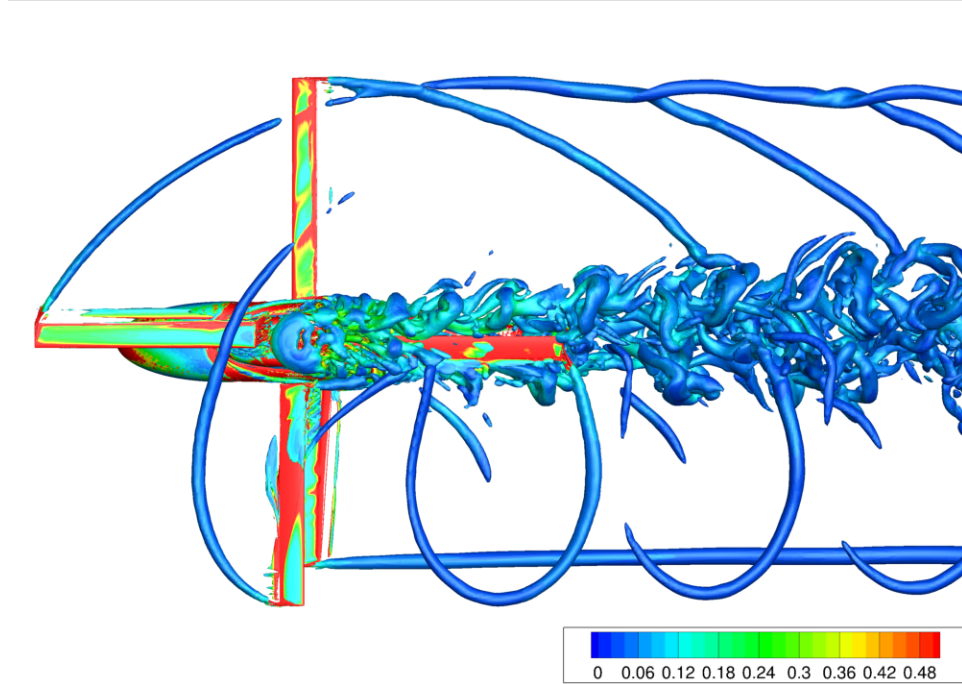
Figure 3.4: Top view of wing-trim case wake visualization using Q-criterion at $\mu = 0.5$ with vorticity shading.

3.2.2 Target C_T

Using the trim for target θ_0 the tonal noise corresponding to the experimental results was found, however, in order to have a fair acoustic comparison it is evident that the two configurations should be trimmed to achieve equivalent thrust. The normal-trim configuration at 10° collective was set as the reference case and a new trim was performed for the wing-trim case using CFD/CSD coupling with the target of achieving the same mean thrust and maintaining the pitching and rolling moments at zero. The convergence of mean thrust and rolling moment to the target values as well as the corresponding control angles are shown in Figure 3.5, in this figure integer numbers in the x-axis represent a coupling iteration. Figure 3.5 shows that the wing-trim with target C_T case converges satisfactorily after 3 CFD/CSD
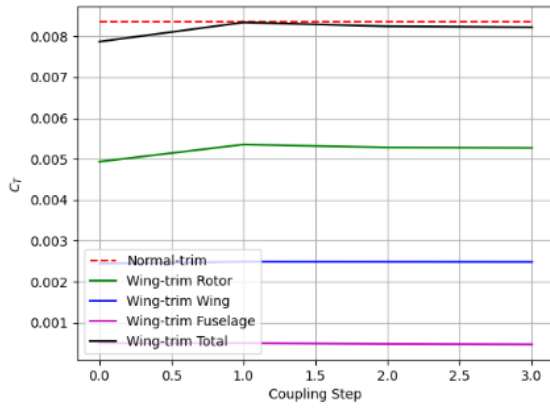
(a) Thrust coefficient convergence.
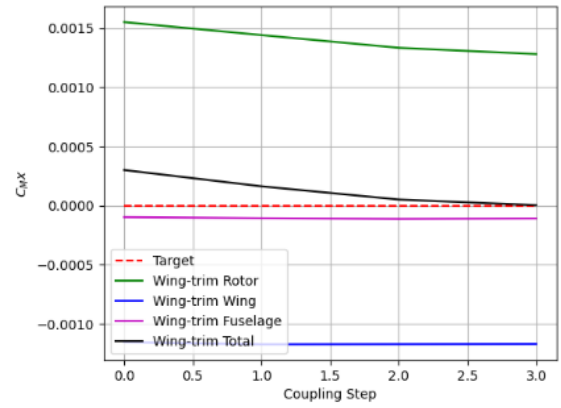
(b) Rolling moment coefficient convergence.
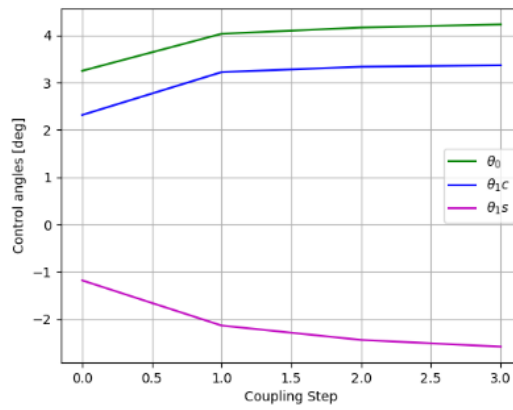
(c) Control angles convergence.

Figure 3.5: Wing-trim at $\mu = 0.5$ CFD/CSD coupling for target C_T convergence.
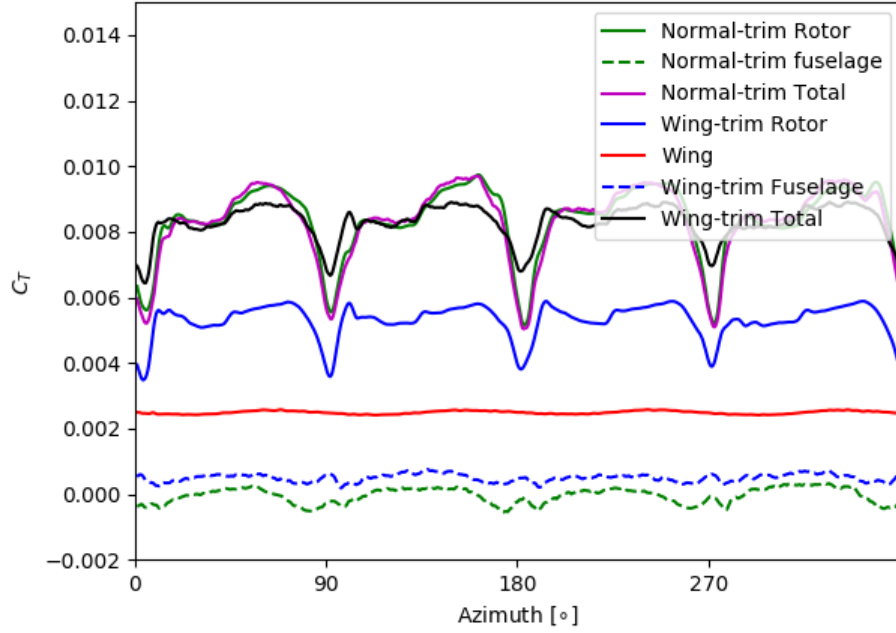
Figure 3.6: Thrust time history of normal-trim and wing-trim cases by component for $\mu = 0.5$ and trimmed for target C_T.

coupling iterations to the control angles seen in Table 3.1. The trim results show that matching thrust allows for the wing-trim case collective to be lowered by more than half as well as a reduction in the longitudinal cyclic magnitude of more than 8°, this larger reduction in cyclic pitch angles will result in less unsteadiness in the thrust production of the rotor.

Figure 3.6 shows the thrust contributions for each component having applied the target C_T trim, the results for the normal-trim case are the same as shown in Figure 3.1 in the previous sub-section. Although the mean thrust values for the wing-trim and normal-trim cases are close, as seen in Table 3.1, the thrust time history shows less abrupt fluctuations from the wing-trim rotor, particularly at 0°, 90°, 180° and 270° azimuth.
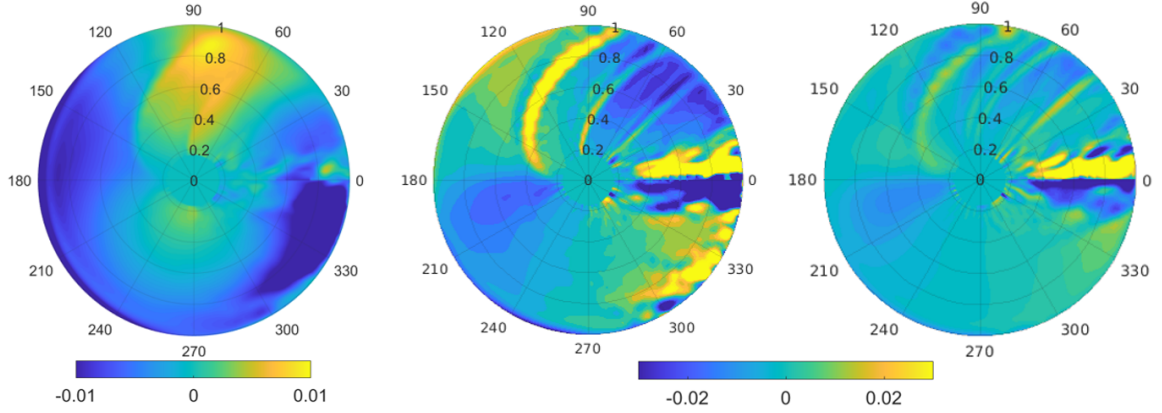
Figure 3.7: Rotor disc contour plots at advance ratio of 0.5: Normal-trim rotor C_N distribution subtracted from Wing-trim rotor C_N with target C_T trim. (left) Normal-trim C_N derivative with respect to azimuth. (middle) Wing-trim C_N derivative with respect to azimuth, target C_T trim. (last)

A closer look at the differences in thrust production and change in thrust on the rotor disc area can be seen in Figure 3.7. These plots have the same scale as the previous rotor disc thrust plots, it can be seen that the rotor produces less thrust throughout most of the rotor disc except the 90° azimuth and the reverse flow region. The target C_T trim also produces less change in thrust with respect to azimuth. It was shown in the previous trim case that a lower thrust does not necessarily result in a lower time derivative of thrust, therefore it is promising to see this large decrease in the time derivative of thrust for the target C_T trim. This smoother thrust production will reduce noise as well as structural vibration from the rotor. The reduced thrust generated by the wing-trim rotor when using this trim condition also helps mitigate the unsteadiness that is generated on the wing due to it being directly under the rotor, a closer look at the difference between the two wing time histories is shown in Figure 3.8. Based on this figure we might expect the noise from the wing of the target C_T case to be less than the target θ_0 case wing.
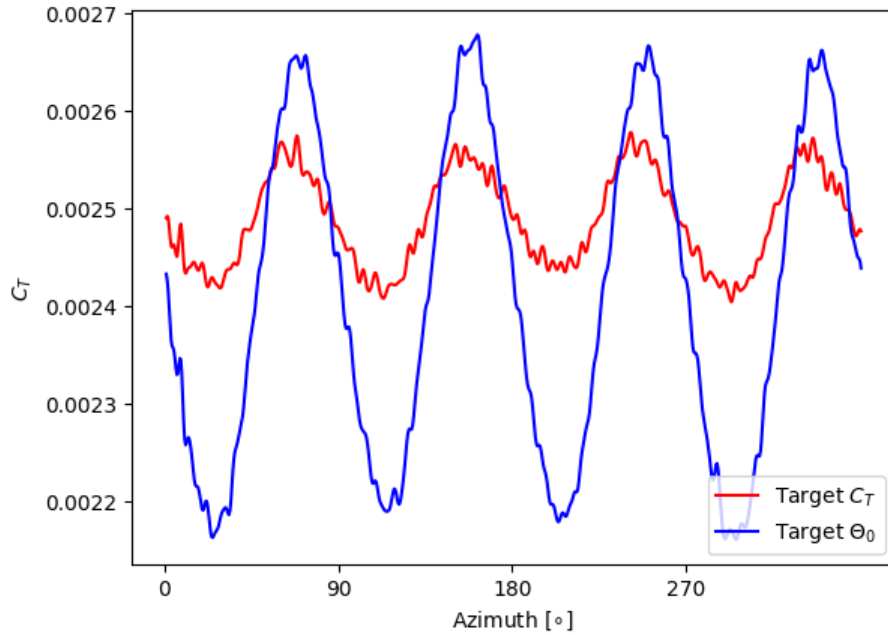
Figure 3.8: Comparison between wing equivalent thrust with target C_T trim and target θ_0 trim at $\mu = 0.5$.

3.2.3 Target C_T with 90% RPM

The intention of this trim condition is to take advantage of the aid of the wing in order to further reduce the RPM of the rotor by 10%, from 700 to 630 RPM. The rotor will have to compensate for the lower rotational velocity by increasing collective, but it will also cause the tip speed to go down. Higher control angles may result in increase noise, and lower tip speed may reduce noise, the dominating effect will be identified. As mentioned previously, instead of maintaining the same advance ratio, it was allowed to increase in order to maintain the 60.3 knots forward flight velocity from the other $\mu = 0.5$ cases. As before, it takes 3 coupling iterations to satisfactorily reach the objectives, the convergence plots are shown in Figure 3.9.
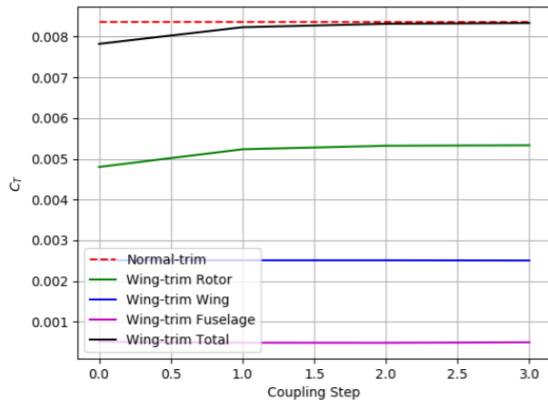
39

(a) Thrust coefficient convergence.
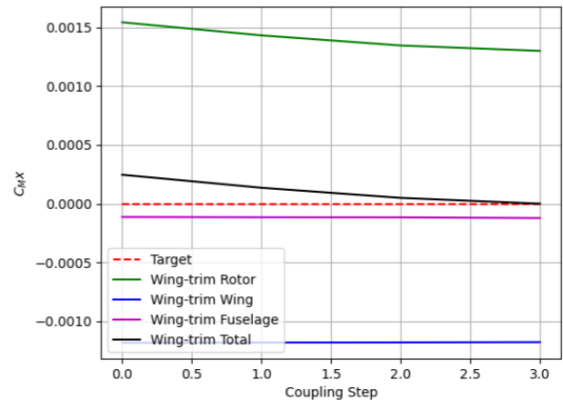
(b) Rolling moment coefficient convergence.
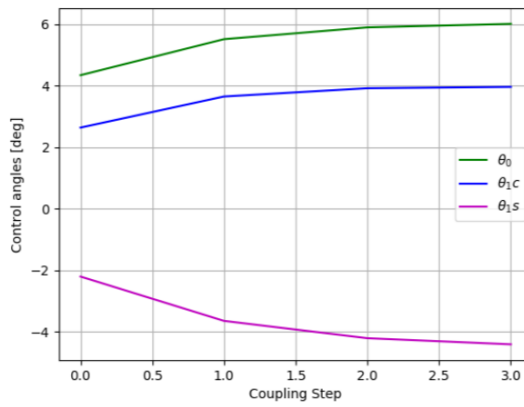
(c) Control angles convergence.

Figure 3.9: Wing-trim at $\mu = 0.55$ CFD/CSD coupling for target C_T and 90% RPM convergence.
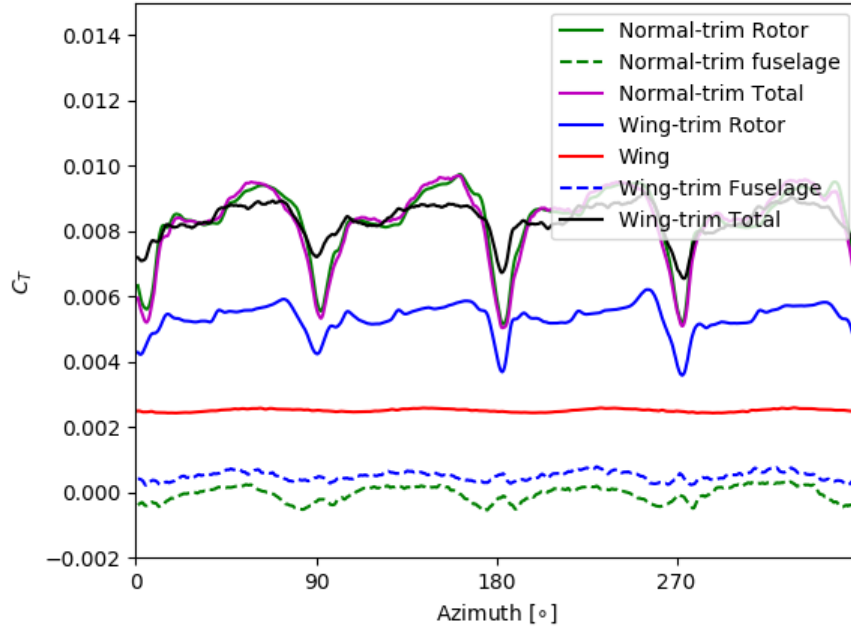
Figure 3.10: Thrust time history of normal-trim and wing-trim cases by component for $\mu = 0.55$, trimmed for target C_T with 90% RPM.

Figure 3.10 shows the thrust time histories for the different components of the aircraft. The thrust production of the rotor for this case behaves in a similar way to that of the target C_T case with 700 RPM. The oscillations from the rotors are similar even though the 90% RPM case has higher control angles, therefore we might expect a similar noise production. However, when we also consider reduced tip speed it becomes more likely that the noise will be reduced overall. Figure 3.11 shows the disc plots for normal-trim at 0.5 advance ratio and the reduced RPM wing-trim cases. All three of the disc plots look similar to the wing-trim 700 RPM target C_T case, a small difference is that the front-most BVI shows a larger thrust derivative for the reducd RPM case, this makes sense considering the control angles are larger. Upon close inspection of Figures 3.11 and 3.7 we see that the BVI are

41
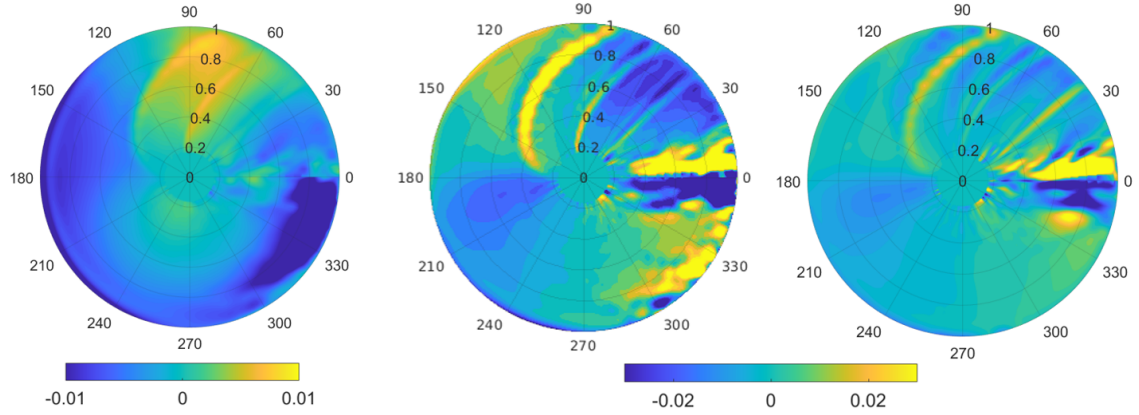
Figure 3.11: Rotor disc contour plots: Normal-trim rotor C_N ($\mu = 0.5$) distribution subtracted from Wing-trim rotor C_N with target C_T trim and 90% RPM ($\mu = 0.55$). (left) Normal-trim C_N derivative with respect to azimuth. (middle) Wing-trim C_N derivative with respect to azimuth, target C_T trim. (last)

slightly further apart for the reduced RPM case, this is to be expected since BVI occur in faster succession to each other at lower advance ratios. It is important to note that the thrust derivative plots shown are with respect to azimuth, not time. This means that the changes in thrust observed in the reduced RPM case happen over a longer period of time than the other cases studied and will therefore have a lower impact on acoustics.

3.3 Advance Ratio of 0.3

When studying this advance ratio, the intention is to compare the aerodynamic and aeroacoustic benefits of the asymmetric wing lift-offset configuration at the two different speeds. Since the wing produces more lift at faster free-stream velocities, it may be expected that a lower advance ratios result in less overall benefits.

(a) Thrust coefficient convergence.

(b) Rolling moment coefficient convergence.

(c) Control angles convergence.
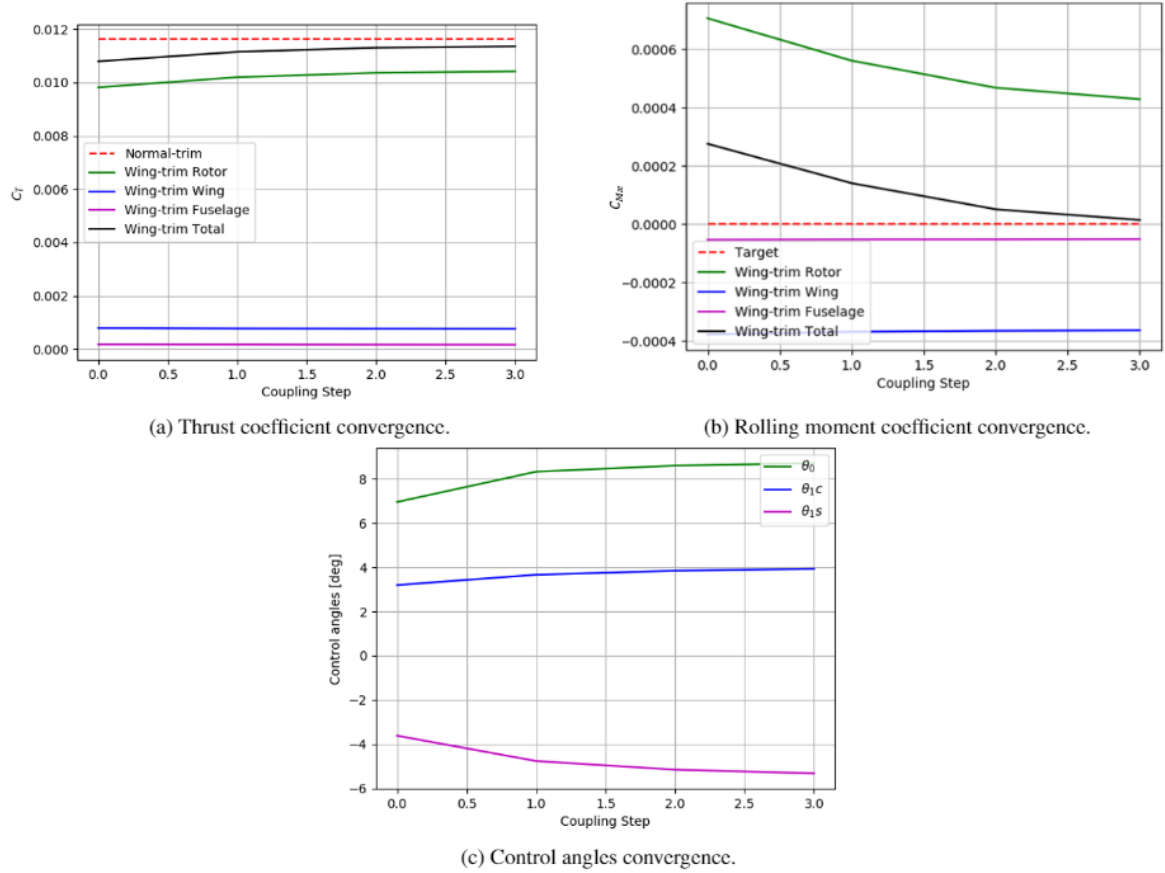
Figure 3.12: Wing-trim at $\mu = 0.3$ CFD/CSD coupling for target C_T convergence.

3.3.1 Target C_T

The final case is at an advance ratio of 0.3. A target trim for equivalent thrust was performed in order to have better noise comparisons between the normal-trim and the wing-trim cases. The convergence plots for the CFD/CSD coupling can be seen in Figure 3.12. The same number of coupling steps where performed as in the advance ratio of 0.5 case. Figure 3.13 shows the thrust time history for the lifting components of the normal-trim and wing-trim cases. Note that the thrust time history looks considerably different than the previous cases at higher forward flight
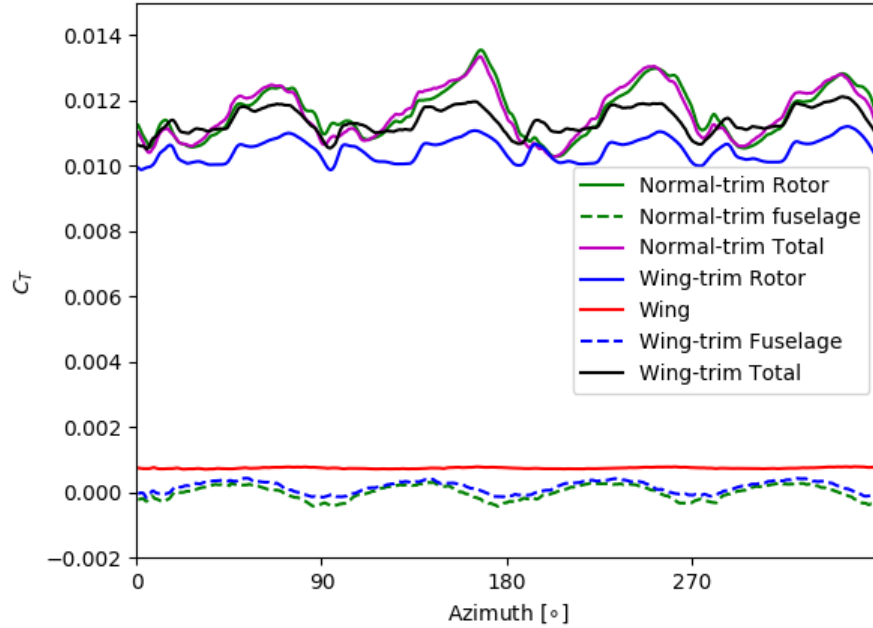
Figure 3.13: Thrust time history of normal-trim and wing-trim cases by component for $\mu = 0.3$ and trimmed for target C_T.

speeds. The rotors are able to produce higher thrust at lower velocities since it is no longer necessary to compensate for the larger reverse flow region. Additionally, since the free-stream velocity is lower, the equivalent thrust generated by the wing decreases substantially. This reduction in wing lift results in the wing producing less than 7% of the total wing-trim configuration thrust. This is a large reduction when compared to the advance ratio of 0.5, where the wing produced 22% of the total wing-trim thrust. Although the wing-trim rotor is no longer producing a large percentage of the thrust as seen in Figure 3.13, we still see that the normal-trim case has larger thrust variations, resulting in more unsteadiness. Considering that similar patterns are observed in a lower scale, it may be expected that at this velocity there will be acoustic benefits, although not of the same magnitude as at the higher
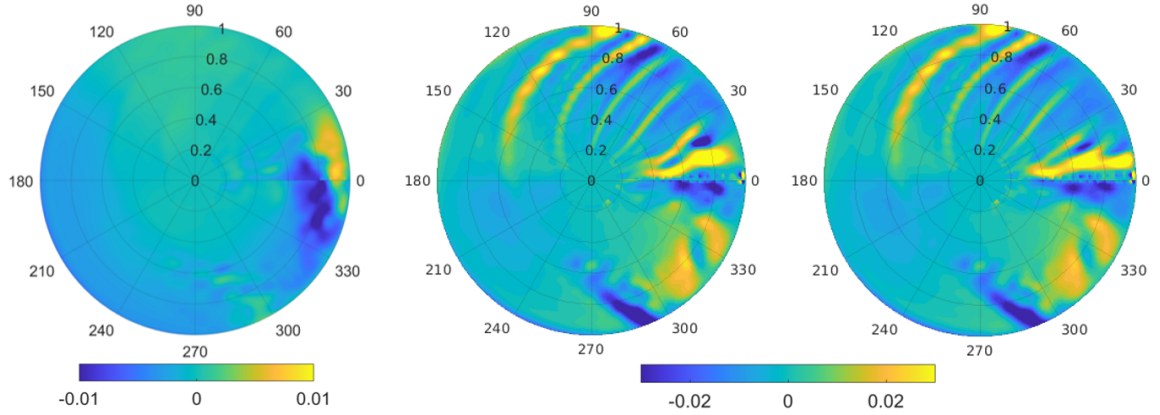
Figure 3.14: Rotor disc contour plots at advance ratio of 0.3: Normal-trim rotor C_N distribution subtracted from Wing-trim rotor C_N with target C_T trim. (left) Normal-trim C_N derivative with respect to azimuth. (middle) Wing-trim C_N derivative with respect to azimuth, target C_T trim. (last)

advance ratio.

Similar observations to those seen in the thrust time history can be made when analyzing the thrust difference for the 0.3 advance ratio normal-trim and wing-trim cases, as well as their corresponding thrust derivatives shown in Figure 3.14. Notice that the difference between the thrust of each rotor is very similar. The thrust derivative with respect to azimuth is only very marginally smaller for the wing-trim case as well. From close inspection of Figure 3.13 we see that, although the normal-trim case evidently has larger oscillations than the wing-trim case, the larger amplitudes are developed more gradually than in previous trim cases. This gradual changes will not show up as clearly in the thrust derivative plots.

Also in Figure 3.14, note that there are more blade vortex interactions occurring in the advancing side. The wake visualization shown in Figure 3.15 explains the reason for the more frequent BVI's. Since the aircraft is now traveling at a lower advance ratio, the tip vortexes trailing from the blades remain on the advancing
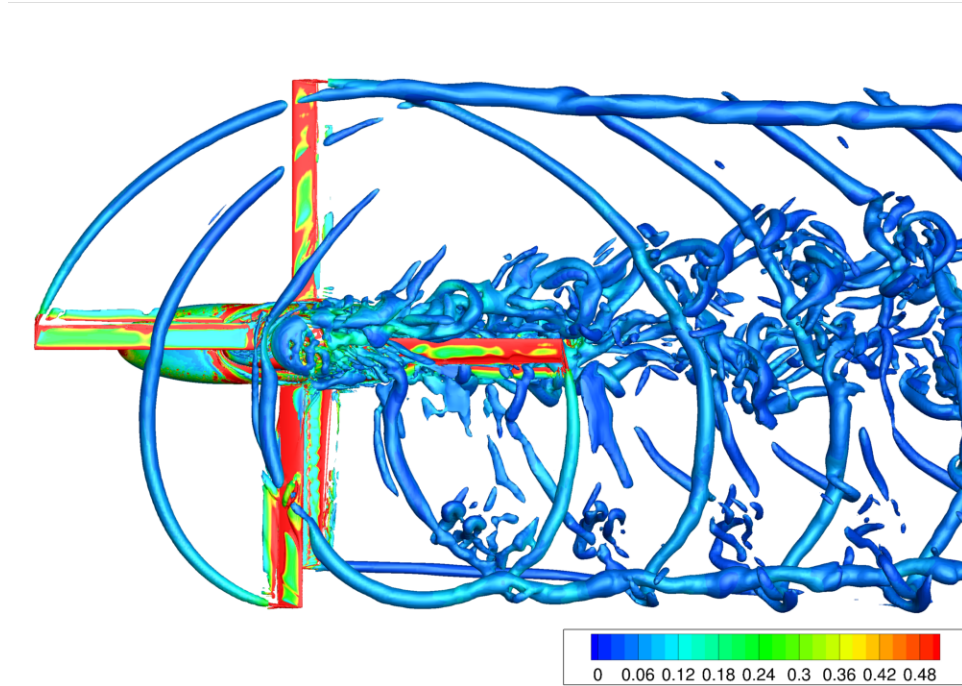
Figure 3.15: Top view of wing-trim case wake visualization using Q-criterion at $\mu = 0.3$ with vorticity shading.

side for longer. This means that a blade traveling through the advancing side will encounter up to five tip vortex structures as seen in the thrust derivative plots. In contrast, at an advance ratio of 0.5 only three clear blade vortex interactions can be distinguished. From Figure 3.15 also note that the regions of high vorticity in the hub wake are less densely packed than at the 0.5 advance ratio. This behavior results in the reduced change in thrust observed at the 0° azimuth for this advance ratio in Figure 3.14.

Chapter 4:   Aeroacoustic Results

Once the aerodynamic results have been obtained we can use them to perform an aeroacoustic analysis of all cases and all components. For each case the tonal noise, and its A-weighted values will be presented. Comparisons will be made between component contributions both within and across cases. At the final section of the chapter there is an analysis of the effects of having wind tunnel walls included in the simulation and the reason for their omission in this study.

4.1   Advance Ratio of 0.5

At this advance ratio all the wing-trim cases are to be compared with the normal-trim case. A comparison of the maximum OASPL of all the components can be seen in Figure 4.1, a more detailed description of each wing-trim case is shown in the corresponding sections. Additional analysis in each section includes the direction of propagation of the noise, frequency analysis, and A-weighted results.

In general, Figure 4.1 shows that in the cases with less variation in rotor thrust generation (see Figures 3.1, 3.6 and 3.10) there is less resultant rotor, wing, and fuselage noise. Although the difference in thrust variations is not that large between the target C_T and 90% RPM case, the reduced tip speed provides additional
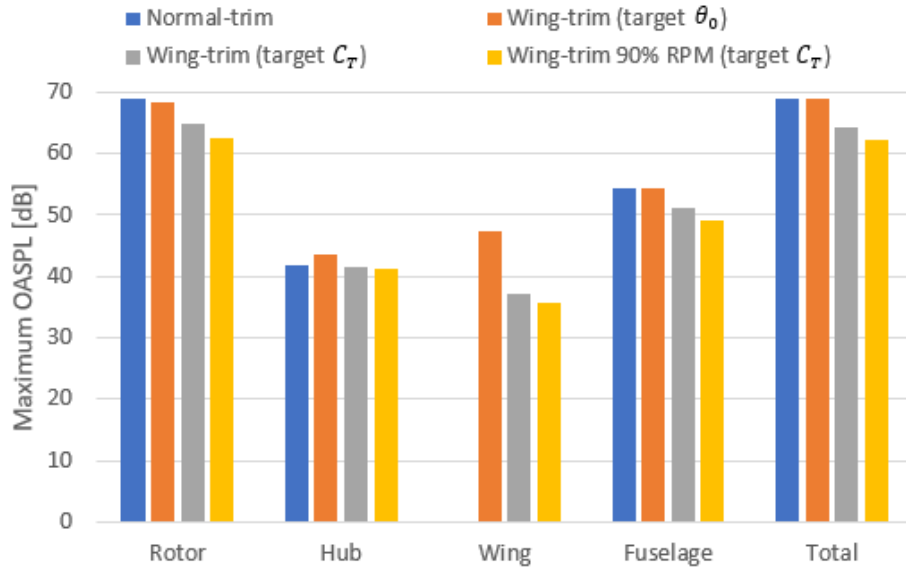
Figure 4.1: Bar graph comparing normal-trim and wing-trim maximum OASPL by component at an advance ratio of 0.5 (0.55 for 90% RPM case).

noise reduction for these components. The acoustic pressure time history at the observer with the maximum OASPL for the rotor of the configurations at 0.5 and 0.55 advance ratios is shown in Figure 4.2. Note the dominant 4/rev signal due to the four bladed rotor and the large differences between cases. The differences in acoustic pressure seem to become less when translated into dB due the logarithmic nature of the unit.

Figure 4.3 shows the acoustic hemispheres under the aircraft for the normal-trim case for a more accurate comparison between the components in the following sections. The maximum OASPL results for the loading OASPL for all cases at $M_{inf} = 0.0911$ are presented in Table 4.1 in both dB and dBA for comparisons between trim conditions in future subsections.
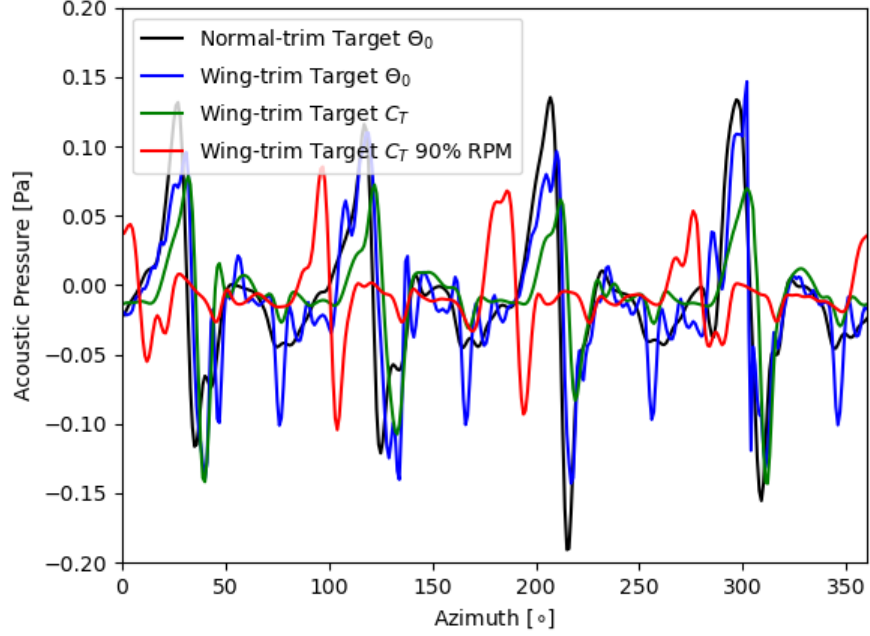
Figure 4.2: Acoustic pressure time history in Pa at the observer with maximum OASPL for the rotor of all $\mu = 0.5$ cases (0.55 for 90% RPM case).

Component	Normal-trim		Wing-trim target θ_0		Wing-trim target C_T		Wing-trim target C_T 90% RPM	
	dB	dBA	dB	dBA	dB	dBA	dB	dBA
Rotor	68.8	56.5	68.4	59.0	64.8	53.8	62.4	50.6
Fuselage	54.5	41.9	54.4	40.3	51.2	41.8	49.1	38.8
Wing	-	-	47.5	22.8	37.2	22.1	35.7	18.9
Hub	41.7	30.5	43.6	32.2	41.4	31.5	41.1	27.9
Total	68.8	56.0	68.9	58.9	64.4	53.6	62.3	51.4

Table 4.1: Maximum loading OASPL of all trim conditions at an advance ratio of 0.5 (0.55 for 90% RPM case).
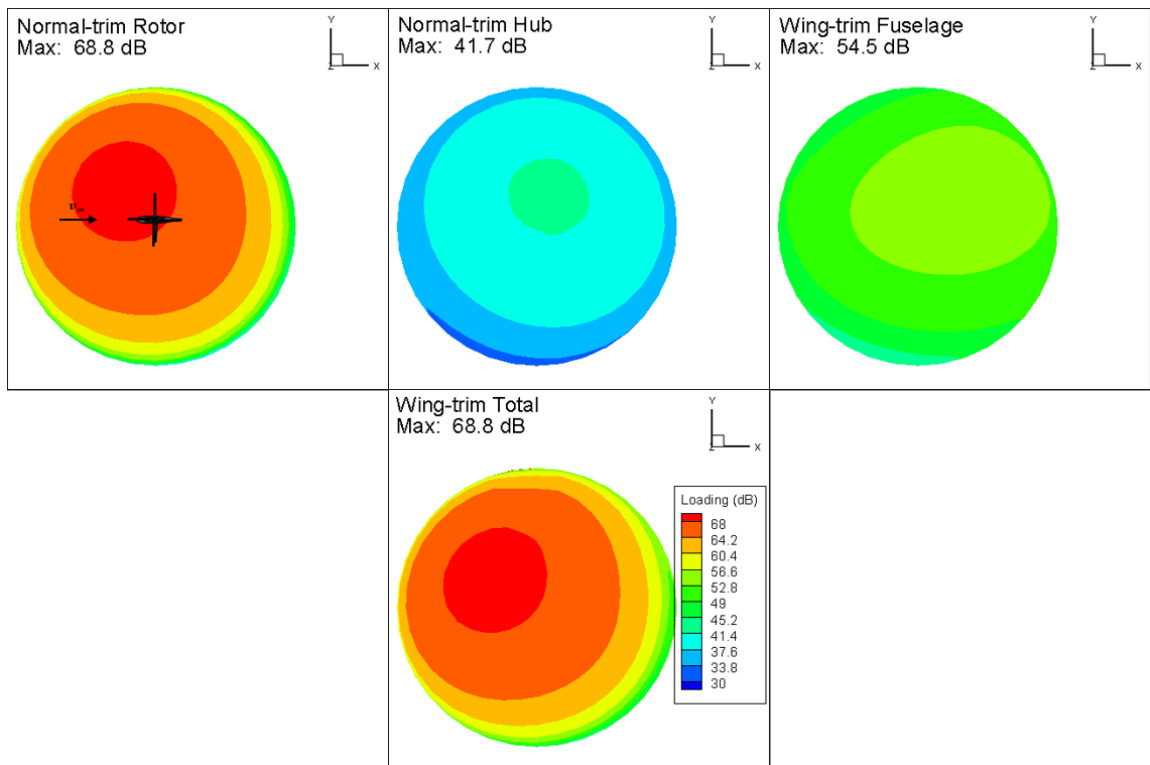
Figure 4.3: Loading noise OASPL (dB) for normal-trim case trimmed for target θ_0 and $\mu = 0.5$.

4.1.1 Target θ_0

The OASPL contour for the wing-trim for target θ_0 case can be seen in Figure 4.4. The vehicle is drawn after scaling up for better understanding of the relative positions of the observers which are located at 30 rotor radii from the rotor hub. The contour shows loading noise OASPL in dB, and the free-stream comes from the left side of the page in all the plots. The thickness noise is not included in these plots since its results do not give relevant contributions to the total noise in any of the cases. At the advance ratio of 0.5 with target collective trim, the wing-trim rotor produced a maximum thickness noise OASPL of 22.5 dB, which is negligible when compared to the 68.4 dB maximum loading noise OASPL produced by the same rotor.

Comparing the loading noise from the rotors of the wing-trim and normal-trim case, we see that both generate similar maximum noise levels, only 0.4 dB higher for the normal-trim case. Even though the wing-trim rotor produces 21.9% more thrust, it still manages to generate slightly less noise due to the reduced cyclic pitch angles. The maximum noise from the hub of the wing-trim case is about 2 dB higher than that of the normal-trim case, the higher thrust from the rotor may be contributing to more unsteadiness on the hub surface. It is important to note that the hub noise for both cases is 25 dB or more below the rotor noise, this means that the hub will have essentially no impact on the total noise of either configuration. The noise from the fuselage (not including wing) for both the cases is very similar, only 0.1 dB higher for the normal-trim case. The fuselage noise is more significant
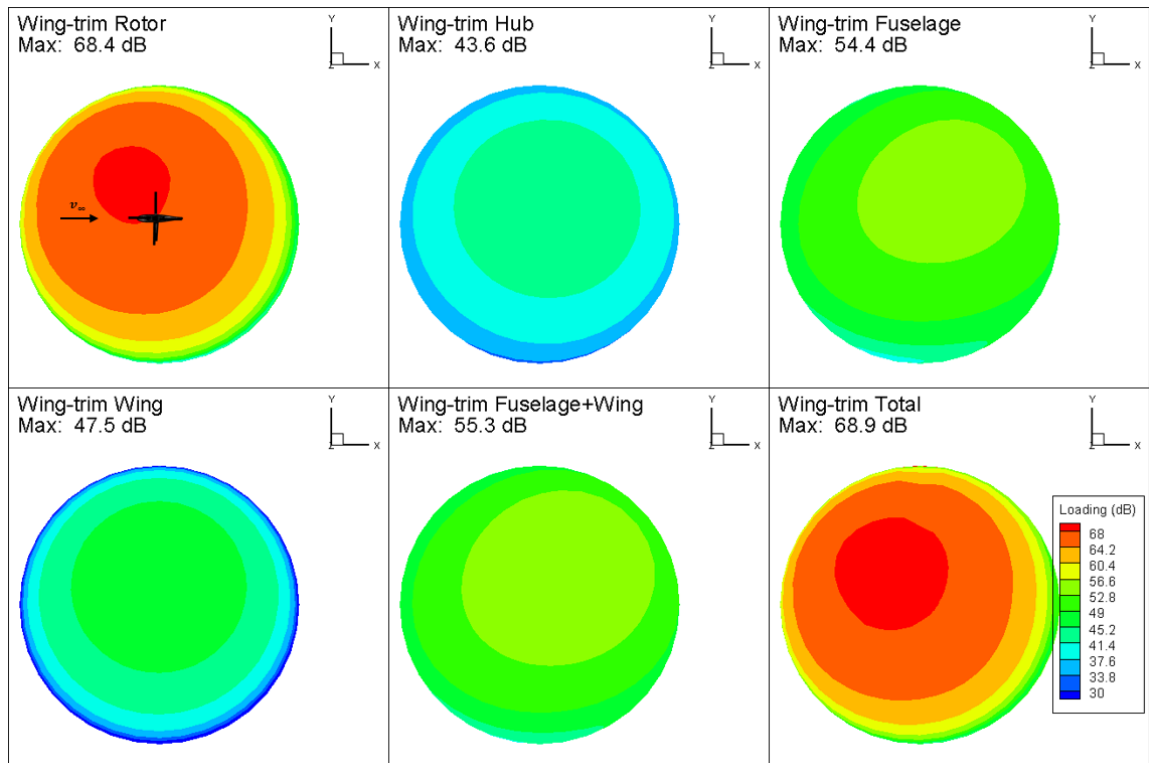
Figure 4.4: Loading noise OASPL (dB) for wing-trim case trimmed for target θ_0 and $\mu = 0.5$.

than the hub noise, but is still almost 15 dB below the rotor noise, once again this will prevent this component from having an important impact on the total noise of the configurations. The maximum noise generated by the wing is larger than the hub noise and lower than the fuselage noise, and therefore also does not have a substantial effect on the total OASPL. This is where the wing-trim case gains the most advantage over the normal-trim in acoustic terms, since the wing contributes a lift-offset and close to 20% of the total lift of the wing-trim case with effectively no acoustic penalty.

The shape of the rotor OASPL hemisphere plot was explained in 3.2.1 by looking at the thrust derivative on the rotor disc. The maximum noise for the rotor disc is observed to occur in front and to the advancing side of the rotor as it would be expected from BVI disturbances in the first quadrant of the rotor disc. The noise for the fuselage is biased towards the rear of the aircraft due to the interactions of the fuselage with the wake of the rotor and hub behind the helicopter.

Performing an FFT on the acoustic results allows us to determine the dominant frequencies at which the different components studied produce noise. Figure 4.5 shows the SPL for a range of frequencies from 0-250 Hz, the figure includes the rotor, fuselage, and wing. The black dotted lines indicate the BPF of the rotor and its multiples. Note that the maximum SPL does not occur at the BPF, and instead is seen at twice the BPF. This is because at high advance ratios BVI and interactions with the hub wake become a dominant source of noise which occurs at higher frequencies. The fuselage noise is largest at the BPF since the fuselage noise depends mostly on the pressure fluctuations caused by the blades passing over it.
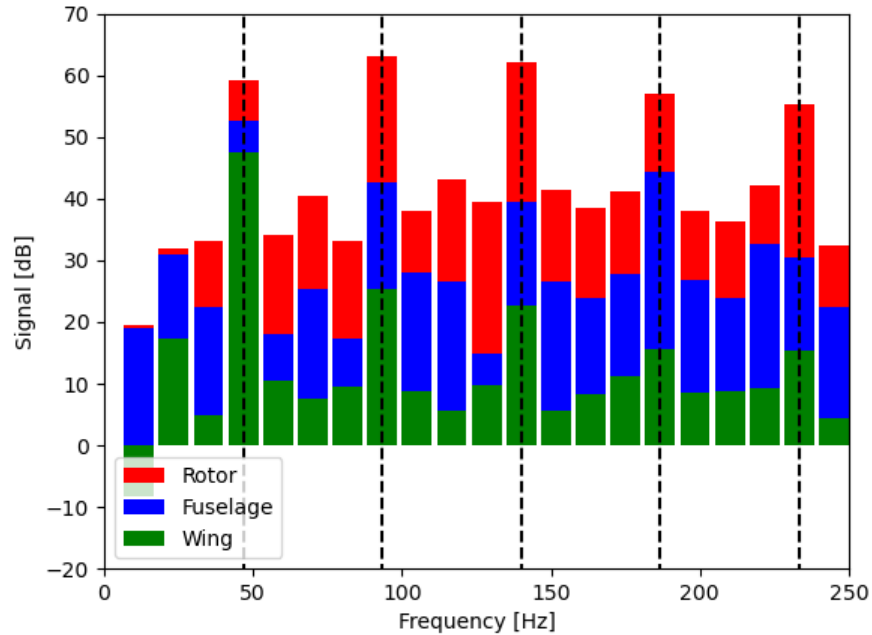
Figure 4.5: SPL by frequency in dB for all rotor, fuselage and wing of wing-trim case with target θ_0 at an advance ratio of 0.5.

There is however, a significant amount of noise occurring at higher frequencies for the fuselage, this is because it impinges on the wake of the rotor and the hub as it can be appreciated in Figure 4.6. The wing also displays a majority of its noise production at the BPF since it also depends on the passing of blades overhead, since it does not impinge on the wake there are no substantial higher frequency signals.

A summary of the acoustic results can be found in Table 4.1, the results show both dB, and the resulting dBA after applying an A-weighting. Note that the loading noise for all components is reduced considerably when performing an A-weighting, this is because loading noise dominates at lower frequencies which the human ear cannot perceive as well. Components which showed higher frequency noise in Figure 4.5, like the rotor and fuselage, have higher A-weighted noise results than the wing,
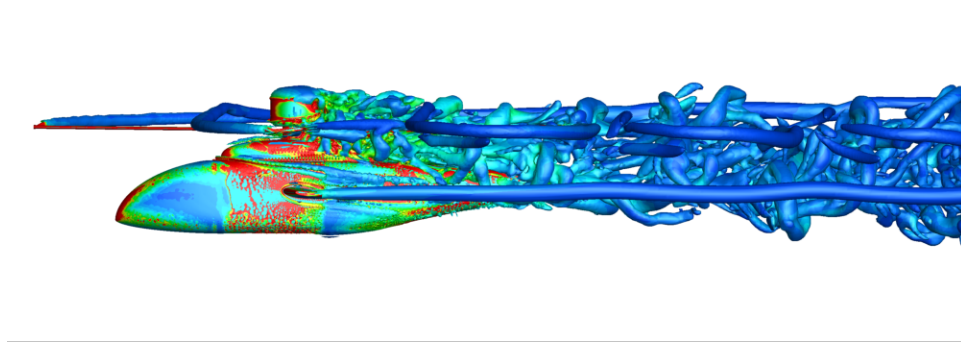
Figure 4.6: Side view of wing-trim case wake visualization using Q-criterion at $\mu = 0.5$ with vorticity shading.

which has most of its noise occurring at the BPF. When A-weighting is applied, the rotor, fuselage, wing, and hub see a 9.4, 14.1, 24.7, and 11.4 dB noise reduction respectively. So the wing tonal noise is much lower than the rotor already, and even less will be perceived by the human ear due to its low frequency noise.

4.1.2 Target C_T

As mentioned previously, the wing-trim case for target C_T was created in order to have a fair comparison between the normal-trim and wing-trim configuration that was not available in previous studies. Figure 4.7 shows the maximum OASPL contours for this trim condition.

The maximum loading noise produced by the target thrust wing-trim rotor is about 4 dB lower than the normal-trim rotor (and therefore the target collective wing-trim case). The hub noise is reduced by 2 dB when compared to the target collective wing-trim case. The target thrust hub is also now slightly lower than the normal-trim hub. This result reinforces the idea that the hub noise is tied to the rotor thrust production, although not in a proportional manner. The lower rotor
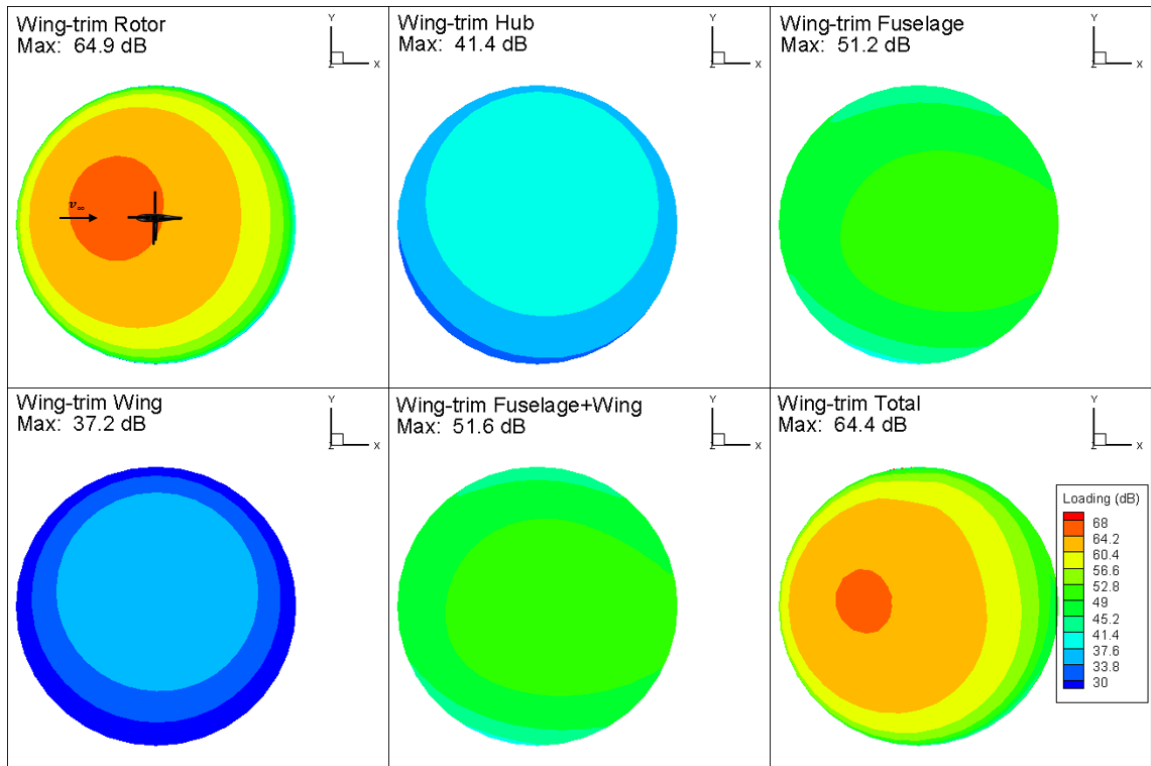
Figure 4.7: Loading noise OASPL (dB) for wing-trim case trimmed for target C_T and $\mu = 0.5$.

thrust also contributes to a 3 dB noise reduction in the maximum fuselage noise. The wing noise showed the largest change with the target thrust trim. The wing maximum OASPL was reduced by 10.3 dB from the previous trim. The reason for this large difference is explained by the reduced unsteadiness in the wing lift seen in Figure 3.8. Due to the large decrease in the wing noise, we also see a smaller difference when adding the noise from the fuselage and the wing together to find the total noise generated by the body of the aircraft. In the target collective case the addition of the wing noise to that of the fuselage caused the total body noise of the wing-trim case to rise a full dB over the normal-trim fuselage, in the target thrust case however, the wing only contributes 0.4 dB to the body noise. When adding all of the components together we notice that the total noise comes out to be 0.5 dB lower than the wing-trim rotor alone, this is an example of destructive noise addition. The results show that at an advance ratio of 0.5, when the wing-trim configuration has total thrust levels equivalent to the normal-trim case, the wing-trim case is capable of operating 4 dB quieter.

An FFT analysis and A-weighting were performed on the target C_T trim as well. The results of this analysis, as well as a summary of the maximum OASPL, results are shown in Table 4.1. The bar plots with the frequency information are displayed in Figure 4.8. From the table we see that the rotor of the target C_T configuration experiences a similar decrease in noise as the target θ_0 case after A-weighting, meaning that the noise reduction achieved with this trim will be noticeable by human observers. The wing and fuselage behave differently, although there is a clear noise reduction in maximum OASPL for these components, the A-weighted OASPL
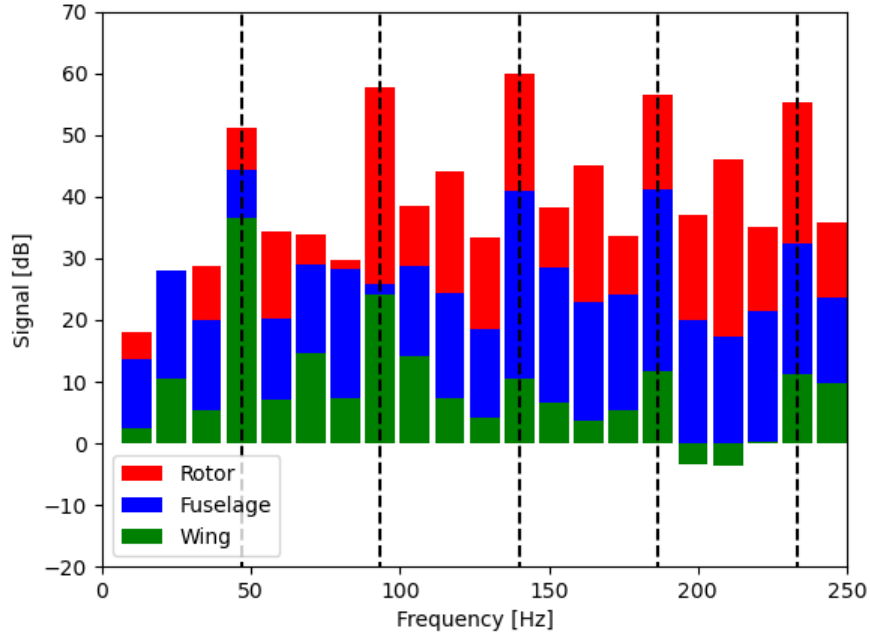
Figure 4.8: SPL by frequency in dB for all rotor, fuselage and wing of wing-trim case with target C_T at an advance ratio of 0.5.

remains similar to the target C_T case. This is because the reduced thrust from the rotor reduces the noise from the components under the rotor mainly at the BPF, while higher frequencies do not experience the same noise reduction.

4.1.3   Target C_T with 90% RPM

The wing-trim case with target C_T and reduced RPM attempts to reduce the noise generation of the helicopter by reducing the tip speed at the expense of an increased advance ratio. The aerodynamic results suggested that the acoustic results should be similar or better than the 700 RPM target C_T case.

Like in previous sections, the maximum OASPL for all the components of the helicopter are shown in Figure 4.9. The rotor experiences a further reduction in
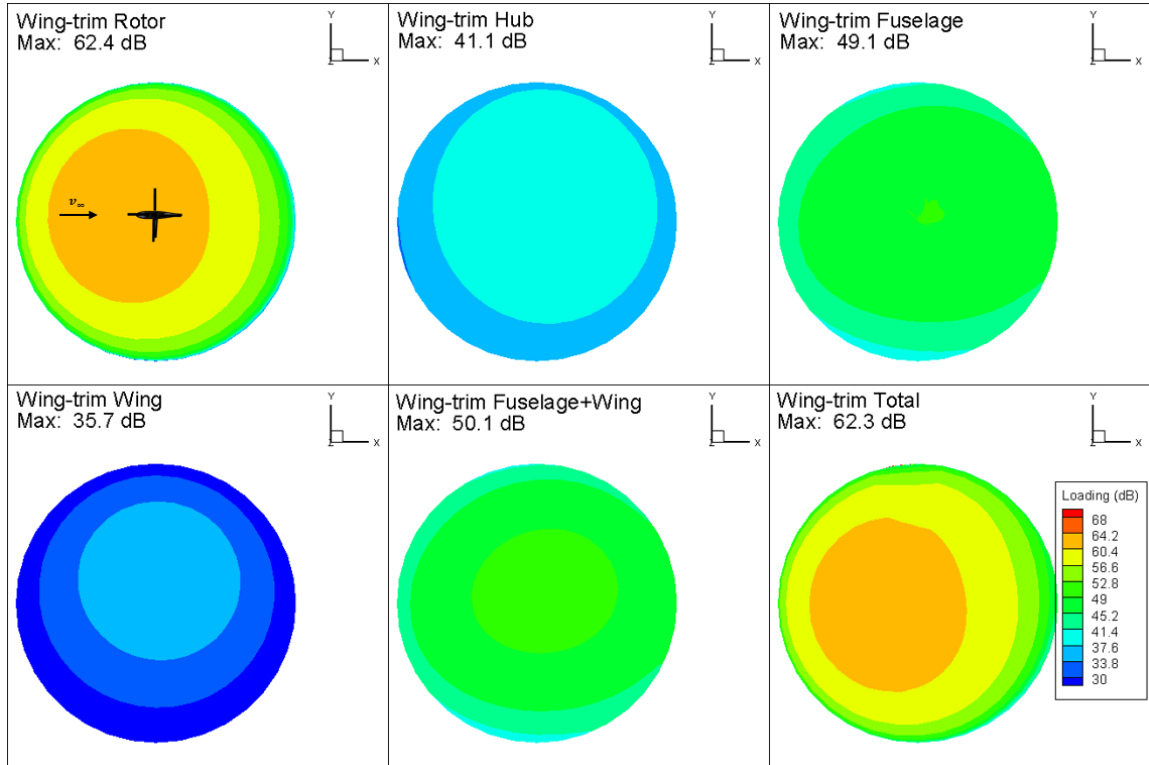
Figure 4.9: Loading noise OASPL (dB) for wing-trim case trimmed for target C_T, 90% RPM and $\mu = 0.55$.

maximum OASPL of 3 dB from the 700 RPM target C_T case, this adds up to a 6 dB maximum OASPL reduction when compared to the normal-trim case. This additional noise reduction comes despite the thrust production time histories being similar for the target C_T cases at the two rotational speeds. The difference comes in the tip speed of the rotor and the reduced time derivatives of the thrust due to the time of a revolution being increased by 10%. A more detailed description of the aerodynamics was shown in Section 3.2.3. The fuselage and wing maximum OASPL are also further reduced by 2 dB likely due to the reduced thrust time derivatives experienced by the rotor which propagate to the components underneath it as pressure fluctuations. The hub maximum OASPL remains almost unchanged.

As in the previous cases, the non-rotating components and the hub do not produce enough noise to significantly affect the total noise of the configuration. The total noise is therefore almost equal to that of the rotor, and is only lower by 0.1 dB due to destructive noise addition. Considering the reduction in total noise we can conclude that the benefits of the reduction in tip speed are greater than the possible disadvantages of requiring higher control angles.

Table 4.1 contains the loading noise maximum OASPL as well as its A-weighted counterpart for each component. A breakdown of the noise results by frequency can be found in Figure 4.10. Note that the BPF now occur at lower frequencies due to the reduced RPM. When comparing the noise by frequency for the 90% RPM case to the 700 RPM target C_T case, we see that the largest noise reduction occurs at higher frequencies such as five times the BPF. This larger reduction in high frequency noise results in additional rotor noise reduction when applying A-weighting to the results. The rotor now has a reduction of 12 dB instead of the 11 dB reduction found without RPM reduction. Similar observations can be made for the wing, fuselage and hub, which experience a larger noise reduction when A-weighting is applied than in the previous cases.

4.2   Advance Ratio of 0.3

The advance ratio is now reduced in order to determine whether the acoustic advantages differ at lower forward flight speeds. The aerodynamic results indicated that a less substantial reduction in noise could be expected from the wing-trim case
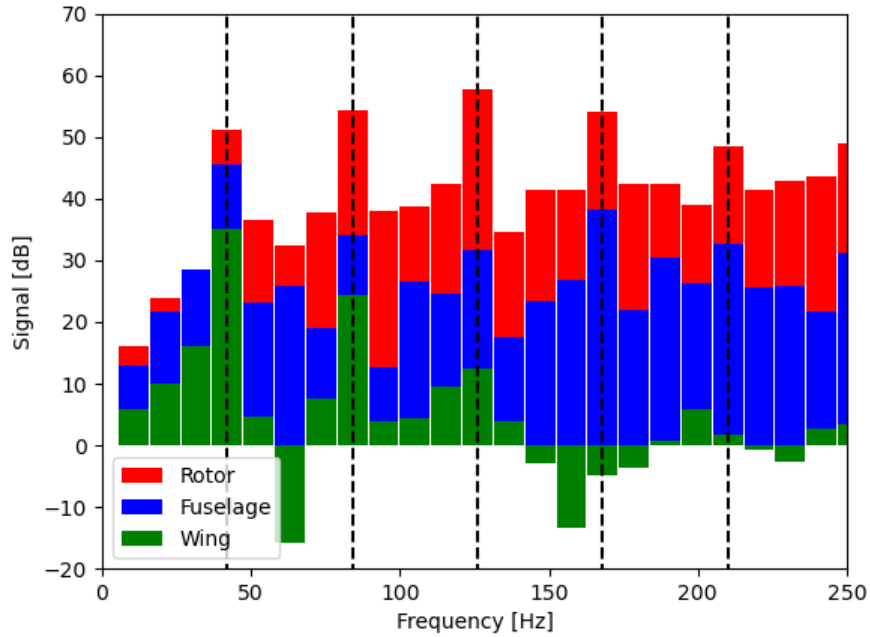
Figure 4.10: SPL by frequency in dB for rotor, fuselage and wing of wing-trim case with target θ_0 at an advance ratio of 0.55 and 90% RPM.

at $\mu = 0.3$. As before, the normal-trim case will be used as a point of comparison. The hemisphere plots for the normal-trim case components can be found in Figure 4.11. At an advance ratio of 0.3 the rotor and total noise are reduced by 5 dB. The fuselage and hub noise are also reduced by 2 dB and 6 dB respectively. The lower forward flight speed results in the first substantial reduction of hub noise so far. The noise is reduced because the variation of the thrust time history is lower, even though higher thrust is being produced. The acoustic pressure time history at the observer with the maximum OASPL for the rotor of the configuration is shown in Figure 4.12. The acoustic pressure is shown at the same scale as in the plot for 0.5 advance ratio, note the overall lower pressure fluctuations, particularly for the larger 4/rev signals.
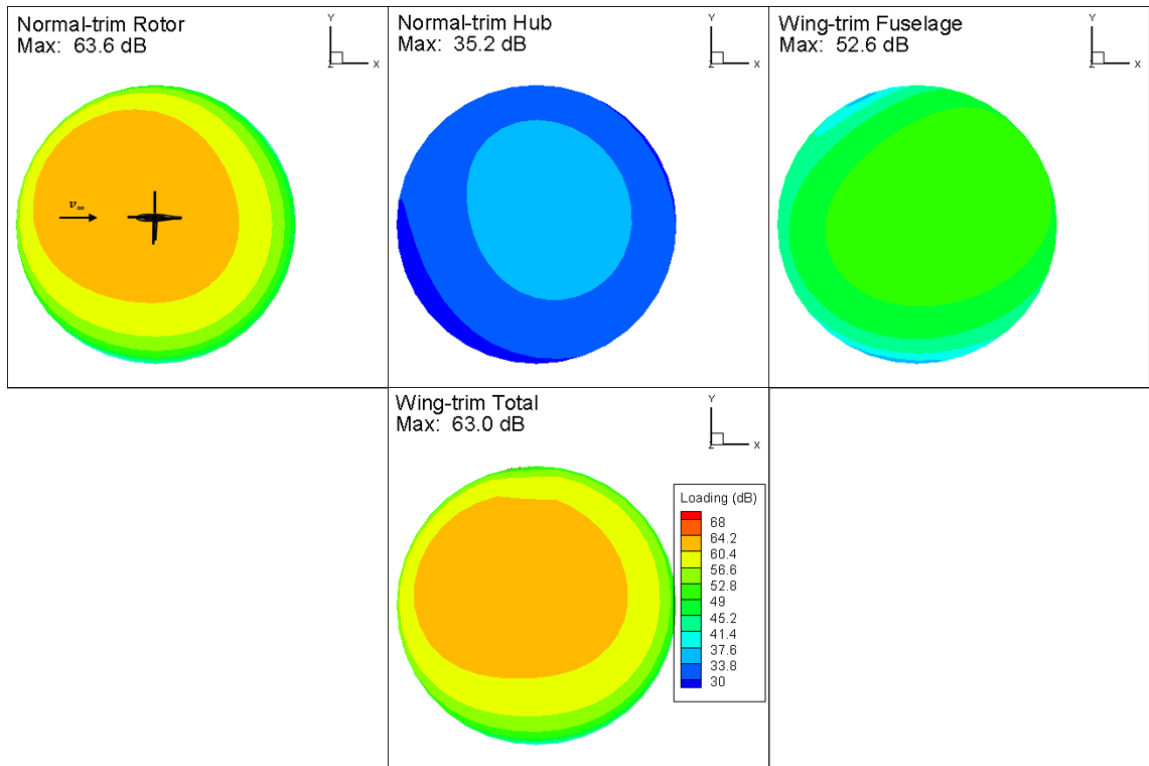
Figure 4.11: Loading noise OASPL (dB) for normal-trim case trimmed for target θ_0 at $\mu = 0.3$.
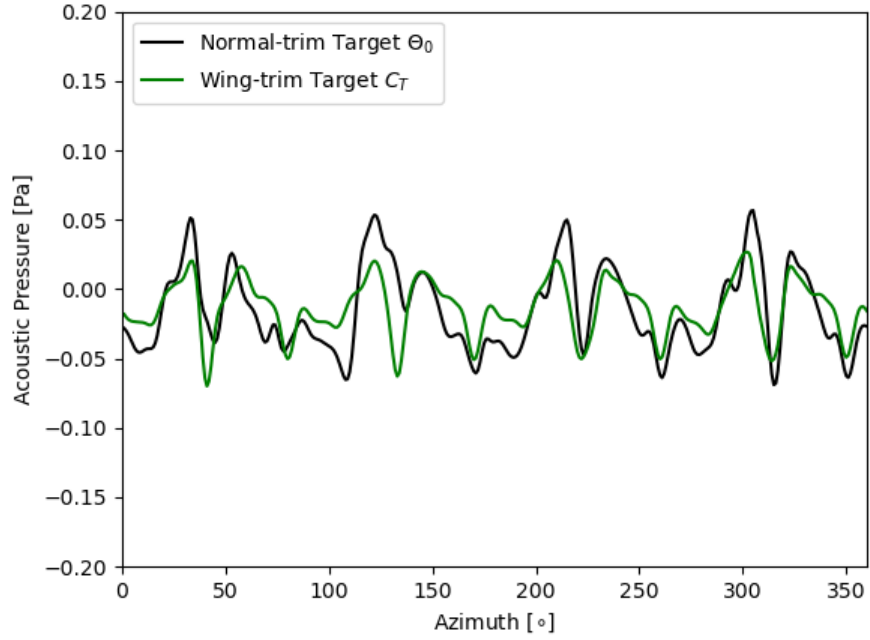
Figure 4.12: Acoustic pressure time history in Pa at the observer with maximum OASPL for the rotor of all $\mu = 0.3$ cases.

Table 4.2 shows the results for maximum OASPL of each case by component and their A-weighted values. In general, at the lower advance ratio there are larger noise reductions when an A-weighting is performed since the noise at higher frequencies is lower. Larger frequency noise is lower because the BVI cause a lower change in thrust time derivative for the normal-trim case at $\mu = 0.3$ as seen in Section 3.3.

4.2.1 Target C_T

The results of matching the normal-trim case thrust with the wing-trim configuration are shown in Figure 4.13. When comparing the advance ratio of 0.3 wing-trim and normal-trim cases, there is a 3 dB reduction in the wing-trim rotor and total noise. This is an important noise reduction, however, it is 1 dB smaller

Component	Normal-trim		Wing-trim target C_T	
	dB	dBA	dB	dBA
Rotor	63.6	49.4	60.0	47.3
Fuselage	52.6	37.5	50.7	35.4
Wing	-	-	31.2	22.0
Hub	35.2	22.2	36.0	23.4
Total	63.0	48.9	60.3	47.6

Table 4.2: Maximum loading OASPL of all trim conditions at an advance ratio of 0.3.
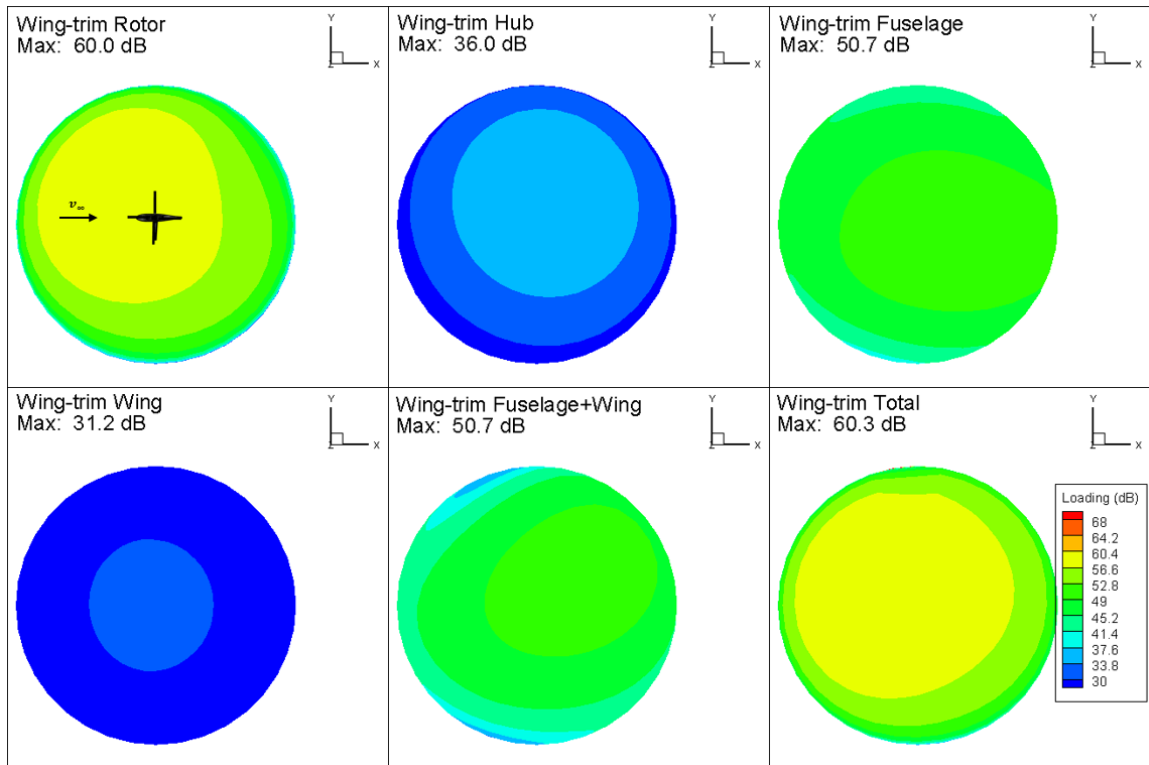
Figure 4.13: Loading noise OASPL (dB) for wing-trim case trimmed for target C_T at $\mu = 0.3$.

than the 4 dB reduction achieved at the 0.5 advance ratio. This indicates that the acoustic advantages of the wing are more noticeable at higher flight speeds. The results found in this case indicate that the rolling moment generated by the wing is more beneficial to the rotor noise than the thrust contributed by the wing. Considering the large reduction in wing lift contribution it may have been expected to see similar rotor noises for the wing-trim and normal-trim cases. The rolling moment provided by the wing also decreases along with the forward flight speed, however, the moment required by the rotor in order to maintain stable flight also diminishes.

The hub and wing are again of no consequence to the total noise of the configuration. It is interesting however to see the wing noise drop to 31.2 dB, lower than in any of the other cases. Although the rotor is producing more thrust in this slower case, the magnitude of the wing thrust is a considerably lower than before and so are the oscillations of the lift time history, this can be seen when closely comparing the wing lift in Figure 3.8 to the aerodynamic results from previous cases. The decreased wing noise causes the normal-trim fuselage to produce more noise than the wing-trim fuselage and wing combined for the first time in the cases studied.

Table 4.2 displays the results of maximum loading OASPL per component and their A-weighted calculations. As we saw for the $\mu = 0.3$ normal-trim case, the wing-trim case also shows a larger reduction in noise when an A-weighting is applied than the $\mu = 0.5$ cases. The SPL by frequency can be seen in Figure 4.14. The noise at higher frequencies behaves similar to the reduced RPM case, showing higher noise reductions at 4 and 5 times the BPF. However, the wing-trim case still show a larger acoustic advantage for the wing-trim cases at $\mu = 0.5$ when comparing
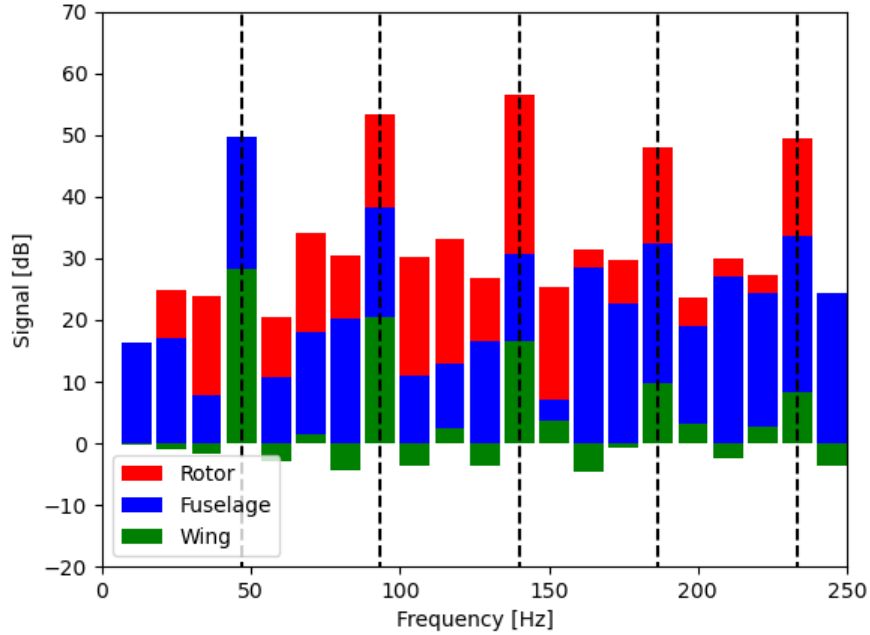
Figure 4.14: SPL by frequency in dB for all rotor, fuselage and wing of wing-trim case with target C_T at an advance ratio of 0.3.

A-weighted results between equivalent advance ratios.

4.3 Effects of Wind Tunnel Walls

As mentioned in Section 2.4, a wind tunnel was initially used in the simulations in order to better match previous experimental and computational studies on the wing-lift offset configuration. It was however found that the wing-trim case experiences substantially increased pressure fluctuations when surrounded by wind tunnel walls, particularly on the fuselage surface. The effect occurred only when a wing was present. In order to further investigate this phenomena, the isolated fuselage for both configurations was placed in the wind tunnel in order to locate the source of the fluctuations. The cowling was removed from both models in order to
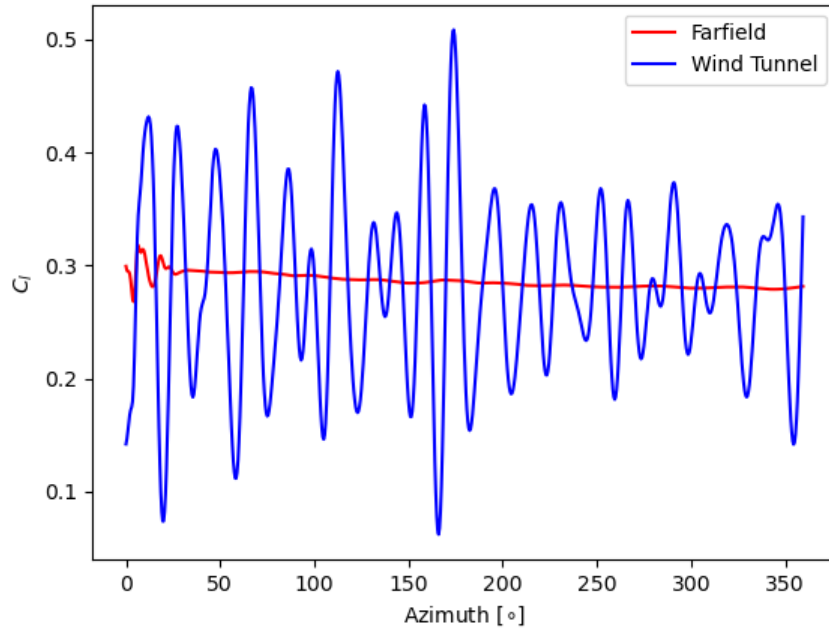
Figure 4.15: Lift time history of isolated wing-trim fuselage with and without wind tunnel walls

eliminate any potential sources of unsteady flow.

It was found that the presence of the stubbed wing on the retreating side caused interactions with the wind tunnel which generated standing waves surrounding the aircraft, these standing waves can be observed in Figure 4.16. The figure shows a snapshot in time of the wing-trim case, a region with increased density approaches the fuselage from the wall. The waves were found to be the strongest at the impulsive start of the simulation and decayed very slowly in time. The normal-trim case did not develop the standing waves when using the wind tunnel walls, therefore the increased fuselage noise affected only the wing-trim case. In order to better compare the fuselage noise from the two configurations, all simulations were performed without a wind tunnel.
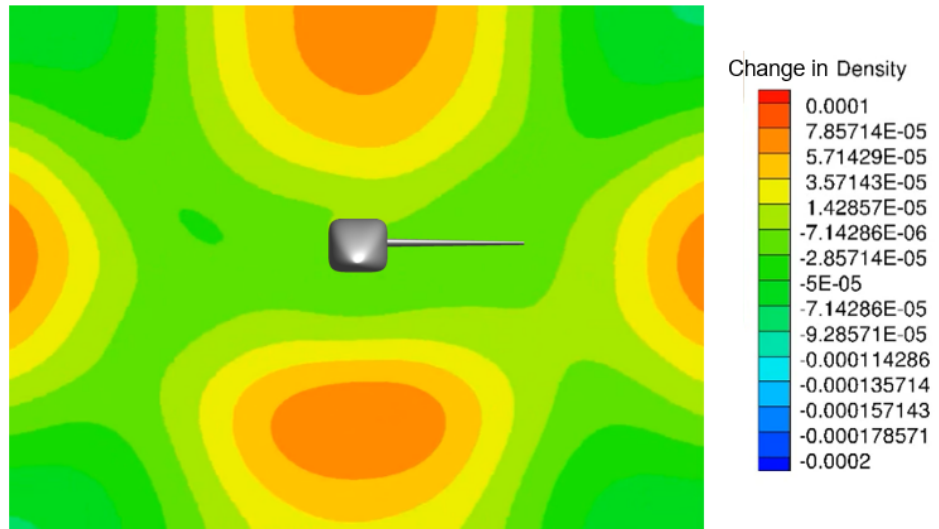
Figure 4.16: Font view of isolated wing-trim fuselage. Snapshot in time of standing waves of increased normalized density change in wind tunnel.

Chapter 5:   Vibratory Loads

It is possible that the reduced aerodynamic loads resulting from the inclusion of a wing on the configuration may cause lower vibratory loads on the rotor. In this chapter, the blade lag and flap bending moments for each trim condition will be analyzed and compared to determine whether the wing-trim configuration also provides an advantage in terms of vibrations. The vibratory loads presented are predictions obtained from the comprehensive code PRASADUM, more details on the structural model are found in Section 2.2.1. The results are presented for both 0.5 and 0.3 advance ratios.

Note that in the structural loads results presented in this chapter, some of the loads have high frequencies and fast responses to aerodynamic loads that may seem atypical for a structural study. It is important to keep in mind that there are fundamental differences in the measurement of structural loads using experiments and computational analysis. When experiments are conducted, the loads are measured with strain gauges. These types of measurements do not respond as fast to aerodynamic loads because they rely on deformations to occur at the location of the gauge. On the other hand, computational analysis utilizes the aerodynamic forces to directly calculate the appropriate moments, this means responses will be faster.

Regarding the high frequency content of the results, particularly in flap bending moment, further studies are being performed to identify the source in the comprehensive code. Despite the fact that the blades may be overly responsive to high frequencies in flap, the results presented for each configuration can be compared relative to each other to find potential advantages.

5.1 Advance Ratio of 0.5

The wing-trim configuration has shown to be consistently more beneficial at higher forward flight velocities, this is why most of the trim conditions studied are performed at the advance ratio of 0.5. The blade flap and lag bending moments can be expected to go down since the wing offloads and offsets the thrust produced by the rotor, allowing it to produce less overall thrust and less rolling moment.

The blade flap and lag bending moment time histories for a full rotor revolution are shown in Figures 5.1 and 5.2. It was found that for similar total thrust production, the advancing side flap bending moment is similar for the different trim conditions. The wing-trim case for target θ_0 stands out with higher advancing side flap bending moment because it is generating higher total thrust than all the other cases. The addition of a wing clearly has a larger effect on the retreating side flap bending moment. The wing-trim cases show a reduction in flap bending moment in the retreating side of the rotor. Even the wing-trim case with target θ_0, which produces more thrust, has a reduced flap bending moment on the retreating side. Both wing-trim cases for target C_T experience very low flap bending moment on

70
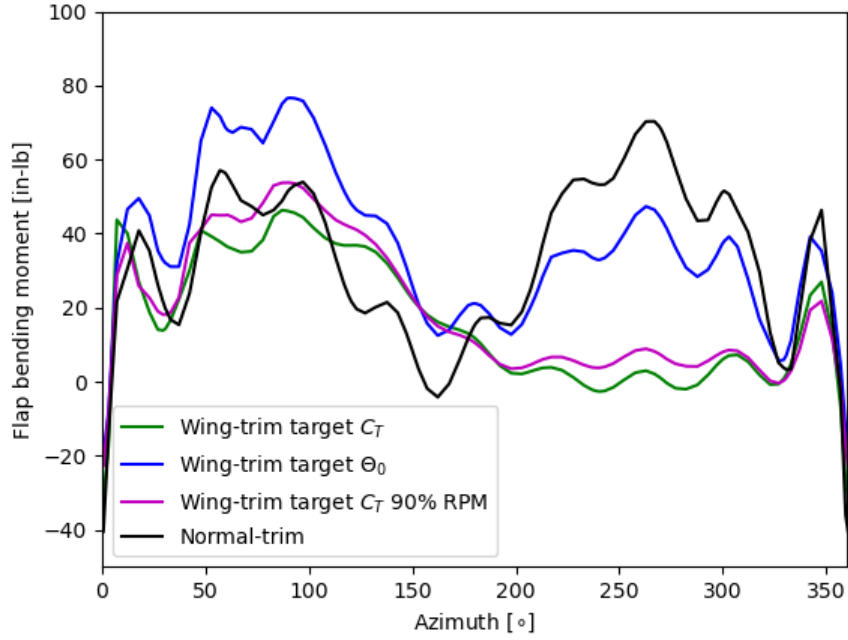
Figure 5.1: Blade flap bending moment for all trim conditions at an advance ratio of 0.5 (0.55 for 90% RPM case).

the retreating side, the reduced RPM case having a slightly larger moment due to the increased control angles necessary. The target C_T cases also show a reduction in the higher frequency oscillations in the moment time history.

Looking at the peak to peak values for the flap bending moment, we find the largest result in the wing-trim target θ_0 case with 116 in-lb. Then next largest peak to peak value is that of the normal-trim case, 110 in-lb. The wing-trim case produces more thrust on the advancing side and the normal-trim case produces more thrust on the retreating side, when comparing these two cases the higher total rotor thrust production from the wing-trim case outweighs the retreating side of the normal-trim rotor resulting in slightly higher vibrations due to flap bending moment. The wing-trim cases for target C_T show the lowest peak to peak flap bending moment values
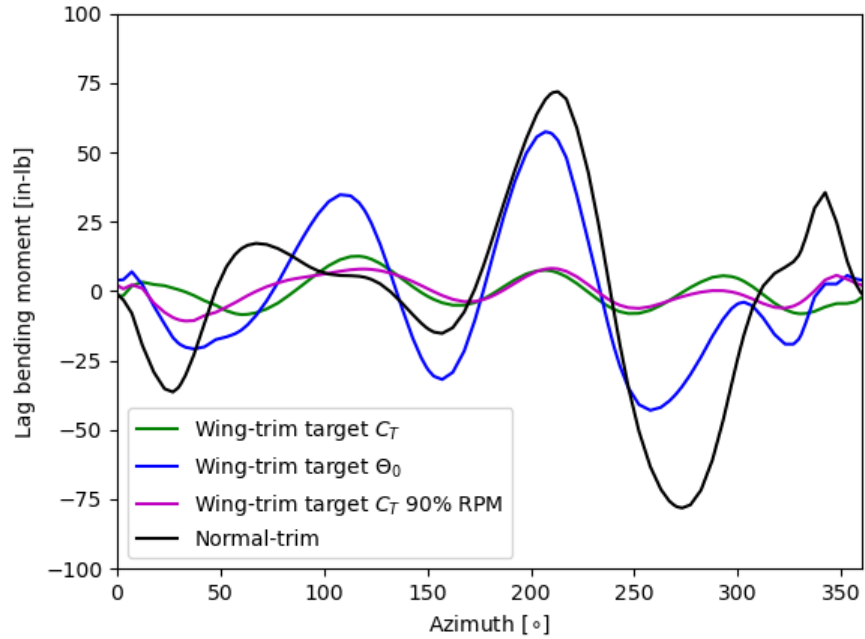
Figure 5.2: Blade lag bending moment for all trim conditions at an advance ratio of 0.5 (0.55 for 90% RPM case).

of 86 and 94 in-lb for the 700 RPM case and for the 90% RPM case respectively. Although this two cases have equivalent rotor thrust production, the 90% RPM case does it with higher control angles, which causes larger vibrations due to flap bending moment.

The wing-trim target θ_0 case shows increased lag bending moment in the advancing side and reduced moments in the retreating side, this results are similar to those seen in the flap bending moment plot. The lag bending moment is substantially reduced for the wing-trim target C_T cases, both the 700 RPM and the reduced RPM case show similar reductions. The normal-trim case has the highest lag bending moment peak to peak value of about 149 in-lb. The wing-trim case for target θ_0, which produces more rotor thrust, follows with a peak to peak value of

99 in-lb. The normal-trim case produces higher vibrations despite its lower total rotor thrust production because it has larger thrust requirements in the retreating side of the rotor. Finally, the lowest peak to peak lag bending moment values are found in the target C_T wing-trim cases, 21 and 18 in-lb for the 700 RPM case and for the 90% RPM case respectively. It is to be expected that the an RPM reduction would somewhat decrease the lag bending moment given an equivalent rotor thrust production.

5.2   Advance Ratio of 0.3

As expected, both the flap and lag bending moments on the blade are lower at reduced forward flight speeds. This means that a smaller reduction in the magnitude of the moments should be expected since the values are smaller to begin with. The blade flap and lag bending moment time histories at $\mu = 0.3$ are shown in Figures 5.3 and 5.4 respectively.

The normal-trim and wing-trim blade flap bending moments show similar trends as in the higher advance ratio, except the wing-trim case for target C_T does not show the same reductions in moment as in the higher advance ratio. For the target C_T case, the results are similar in the advancing side, but the flap bending moment in the retreating side is higher than at the 0.5 advance ratio. This is because the wing is not producing as much lift-offset due to the slower free stream velocity, causing for the blades to experience larger moments particularly in the retreating side. It is also important to remember that the aircraft is producing more thrust
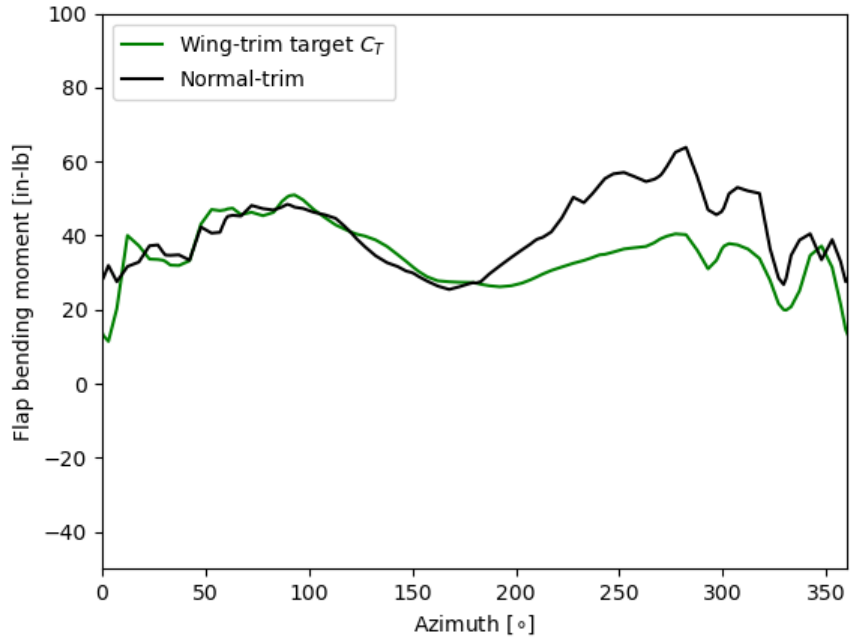
Figure 5.3: Blade flap bending moment for all trim conditions at an advance ratio of 0.3.

at the lower advance ratio. Overall, the high and low frequency oscillations are considerably lower at $\mu = 0.3$. The wing-trim target C_T case and normal-trim cases have similar peak to peak flap bending moment values of 39 and 38 in-lb respectively. Even though the wing-trim case has a reduction in rotor thrust production and control angles, the vibrations due to flap bending moment remain similar at the advance ratio of 0.3.

The results for the lag bending moment are closer in magnitude to those at an advance ratio of 0.5, with the largest reduction occurring at the 210°azimuth. The wing-trim target C_T case shows lower lag bending moment than the normal-trim case, although the difference is less noticeable than at a 0.5 advance ratio. The peak to peak values for lag bending moment are 102 and 65 in-lb for the normal-trim and
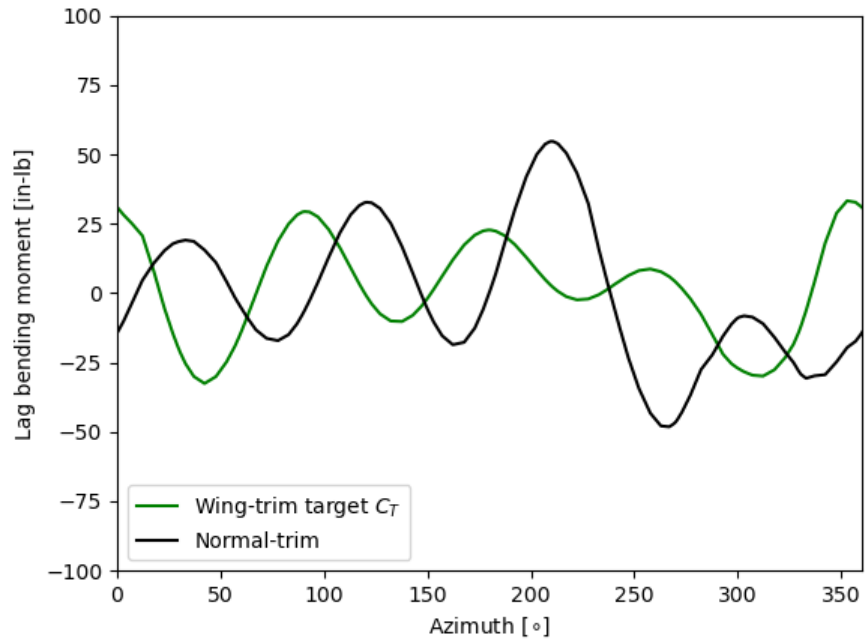
Figure 5.4: Blade lag bending moment for all trim conditions at an advance ratio of 0.3.

wing-trim case respectively. Once again the main difference is at the retreating side were the normal-trim case must produce more thrust to maintain zero rolling moment.

Chapter 6:   Conclusions

Previous numerical and experimental studies on the aerodynamics of the wing lift-offset configuration were replicated using the Mercury CFD framework in order to obtain the surface pressure necessary to conduct an aeroacoustic analysis. Additionally, new trims for the aircraft were developed matching the thrust of the normal-trim and wing-trim cases in order to have a better acoustic comparison, as well as reducing the rotor RPM to better show the potential of the aircraft. A comparison between the normal-trim and wing-trim cases vibratory loads was also performed in order to identify possible additional advantages. This study has found that, in addition to increased thrust potential, the inclusion of a wing also results in noticeable acoustic advantages at high advance ratios.

The results are broken down into the different areas studied in the following subsections.

6.1   Aerodynamics

At an advance ratio of 0.5, it was found that with an equivalent collective angle, the wing lift-offset configuration can produce 56.8% higher total thrust, and 21.9% higher rotor thrust. Although there was an increase in thrust, the thrust time

derivative was found to be similar to that without a wing.

When equivalent total thrust is produced by the wing-trim case as the normal-trim configuration, the collective angle was reduced by more than 50% and the longitudinal cyclic was reduced by over 8°. This resulted in lower thrust time derivative despite the equivalent thrust.

Reducing the RPM by 10% and maintaining equivalent thrust on the wing-trim case resulted in slightly increased control angles but similar oscillations in the thrust time history and thrust time derivative.

Reducing the advance ratio to 0.3 resulted in higher thrust values with smaller oscillations for both normal-trim and wing-trim cases. The wing-trim case with an equivalent thrust still has lower oscillations in its thrust production, however the difference is less noticeable, particularly in the thrust time derivative plots.

6.2   Aeroacoustics

At an advance ratio of 0.5, the wing-trim case with same collective generated a similar maximum total OASPL as the normal-trim case despite producing more thrust. When the wing-trim thrust is matched to that of the normal-trim case, the wing-trim case showed a 4 dB maximum total OASPL reduction. Reducing the rotor RPM by 10% resulted in an additional noise reduction of 2 dB, indicating that the lower tip speed had a larger effect than the increased control angles on the noise.

At an advance ratio of 0.3 the OASPL levels of both configurations was lower.

At this advance ratio the wing-trim case with matched thrust achieved close to a 3 dB maximum total OASPL reduction, which is a significant improvement but is less than the benefits found at the higher advance ratio. The noise reduction in this case is more impressive considering the significantly lower lift being produced by the wing. This case emphasized that, for acoustic purposes, the moment contribution of the wing is more important than its lift contribution.

The interactional aeroacoustic effects between the rotor and wing were found to be minor. In all the cases studied the rotor was by far the dominant source of noise. In all wing-trim cases, the wing was able to provide important aerodynamic advantages without any negative aeroacoustic impact. The low noise generation of the wing is due to its small surface area with respect to the rotor, as well as its position relatively far away from the rotor.

6.3 Vibratory Loads

At an advance ratio of 0.5, it was found that the wing-trim case can produce similar peak to peak flap bending moments and reduced lag bending moments as the normal-trim case despite producing over 20% higher rotor thrust. The wing-trim cases for target C_T showed important reductions in lag bending moment peak to peak values, and slightly lower flap bending moment peak to peak values while producing equivalent total thrust to the normal-trim case. The vibrations were found to be similar between the target C_T 700 RPM and 90% RPM cases for flap lag bending moment, and slightly higher lag bending moment vibrations for the 90%

RPM case.

At an advance ratio of 0.3, the vibrations for both the normal-trim and wing-trim cases were significantly reduced. The reduction in peak to peak values for both flap and lag bending moments between the normal-trim and wing-trim target C_T cases were also reduced, both in magnitude and in percent reduction. Overall, the advance ratio of 0.3 showed significantly lower vibratory advantages than at the higher advance ratio due to the lower lift contribution of the wing on the retreating side.

6.4   Future Work

One of the main limitations of this study is the low tip mach number of under 0.2 experienced by all the cases studied. The forward flight speed and rotor radius and RPM are limited by the wind tunnel facilities and the capabilities of the equipment used in the experiments. Since the study presented relies on the experimental data for performance validation, the acoustic results shown do not occur at realistic tip speeds for a passenger aircraft. Future work could include scaling up the aircraft while conserving the studied advance ratios in order to account for compressibility effects present in larger aircraft. A faster tip speed would also allow for a broadband noise analysis to be appropriately incorporated into the research since it will prevent it from overshadowing other sources of noise.

The wing lift-offset configuration is intended to include a swiveling pusher propeller in order for it to be able to attain the desired forward flight speeds and

counteract the rotor yaw moment. Future work for this configurations includes adding a pusher propeller to the configuration and performing a new high-fidelity aerodynamic and aeroacoustic analysis.

Finally, it would be beneficial if acoustic experiments could be performed for both configurations at the faster tip speed to confirm the acoustic benefits of the wing lift-offset configuration and to validate the tonal and broadband noise predictions.

Appendix A: Broadband Noise

An analysis of broadband noise was conducted in addition to the tonal noise results presented in Section 4. The broadband noise calculations were performed for the rotor of each trim condition studied. The broadband noise results were not included in the main chapters of the paper because the low tip speed used in this study causes the broadband noise to be dominant, this would take away from the relevance of the tonal noise analysis performed which will become the dominant source of noise at more realistic tip speeds. In this appendix the broadband noise results will be presented along with a thought experiment increasing the tip speed of the case in order to provide a demonstration of how the broadband and tonal noise would change in such conditions.

A summary of the broadband noise results can be found in Table A.1, the results are presented in dB and in dBA. Notice that the maximum broadband noise

Trim Condition	dB	dBA
Normal-trim $\mu = 0.5$	67.5	67.7
Wing-trim target $\theta_0, \mu = 0.5$	67.6	67.8
Wing-trim target $C_T, \mu = 0.5$	67.4	67.8
Wing-trim target $C_T, \mu = 0.5$, 90% RPM	67.2	67.8
Normal-trim $\mu = 0.3$	66.1	66.6
Wing-trim target $C_T, \mu = 0.3$	66.6	67.1

Table A.1: Broadband noise results for all trim conditions studied in dB and dBA.
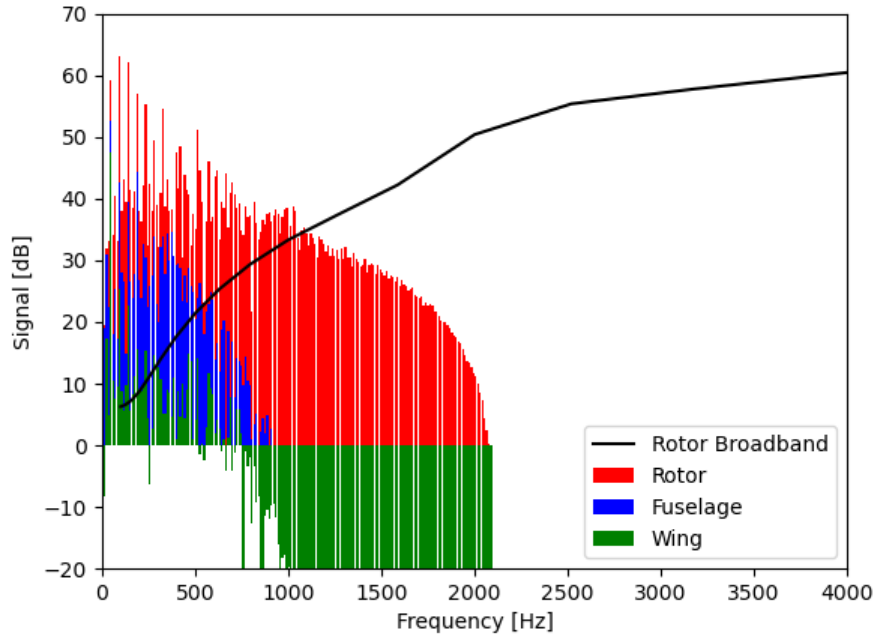
Figure A.1: Broadband rotor SPL and Tonal SPL by frequency in dB for rotor, fuselage and wing of wing-trim case with target θ_0 at an advance ratio of 0.5.

SPL in dB is similar or higher than the tonal noise values in Tables 4.1 and 4.2 for all the cases studied. Also, note that while the loading noise for all components is reduced considerably when performing an A-weighting, the broadband rotor noise increases slightly. This is because broadband noise occurs at higher frequencies which are perceived more by the human ear. Figure A.1 shows the SPL at a larger range of frequencies for the wing-trim target θ_0 case. The figure shows that tonal noise dominates at frequencies below 1000 Hz, and the rotor broadband noise becomes the dominant noise source at frequencies higher than 1000 Hz, which are the frequencies better perceived by humans.

The broadband noise dominates the noise of the cases studied because the tip speed is low, this causes tonal noise to be lower than it would be expected from

a real aircraft, the same reduction is not seen on broadband noise with decreased tip speed. A thought experiment increasing the forward flight speed and tip speed to be three times higher was performed in order to achieve values of tonal noise compared to broadband noise that are more representative of a real aircraft. New CFD simulations were not performed, instead, the same CFD pressure coefficients were used in the acoustic code and the input velocity and tip speed where modified. Changing both forward flight velocity and tip speed allows us to maintain the same advance ratio as in the cases studied. The tip Mach number increased from 0.183 to 0.549 as a result of these changes. Figure A.2 shows the rotor OASPL for the normal-trim case at $\mu = 0.5$ for both tonal and broadband noise at the regular and increased tip speeds. The tonal noise is shown to increase by about 31 dB with three times the tip speed, while the broadband noise only increases by about 6 dB. This difference explains why the broadband noise dominates at low tip speeds but would not dominate at more realistic tip Mach numbers.

Figure A.3 shows a breakdown of the different components in broadband noise for the normal-trim rotor at the two different tip speeds. Notice that the laminar boundary layer noise dominates at both tip speeds, the maximum LBL_VS noise increases by a few decibels with the faster tip speed. The largest changes when tip speed is increased occur for the other sources of broadband noise, there is a substantial dB increase from the TBL, TEB and TVF noise sources of over 15 dB. Although the increased tip speed has a large effect on these components of broadband noise, they are still smaller in magnitude than the LBL_VS noise which does not change as much, this causes the total broadband noise to have a relatively
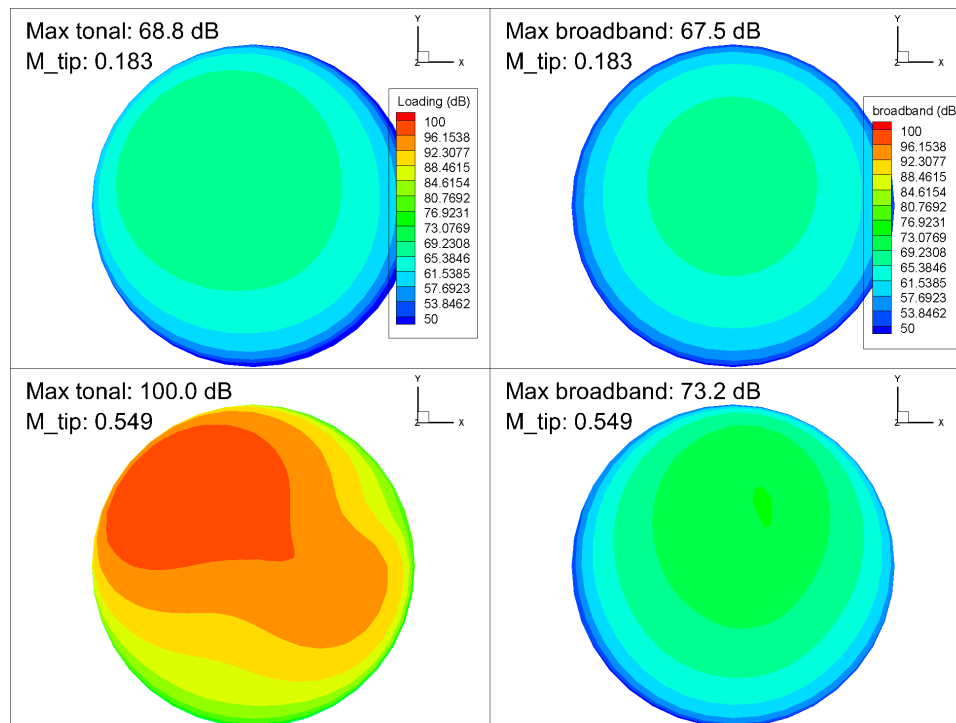
Figure A.2: Broadband (right) and Tonal (left) rotor OASPL in dB of normal-trim case with target θ_0 at an advance ratio of 0.5. Results shown with M_{tip} of 0.183 (top) and 0.549 (bottom)
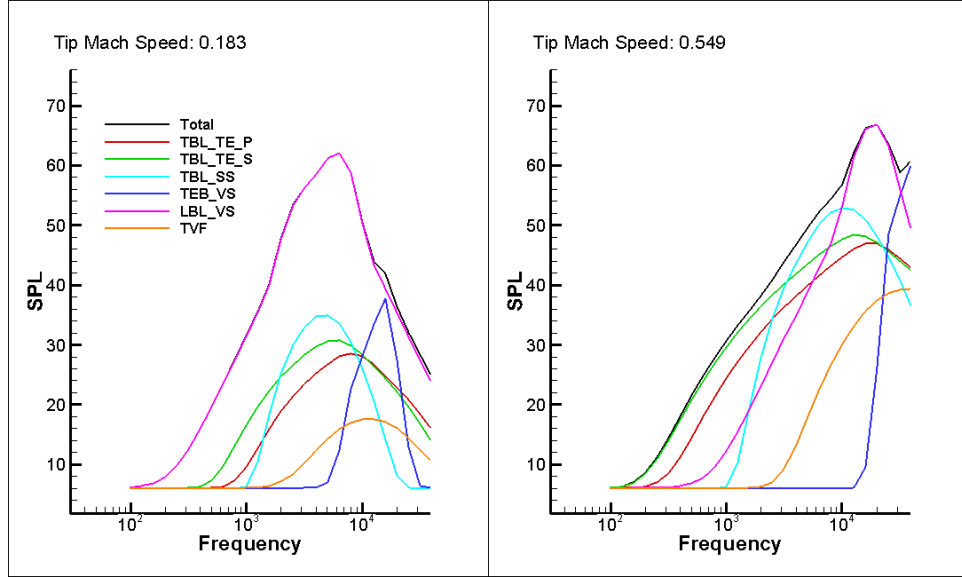
Figure A.3: Rotor broadband noise breakdown into components in dB of normal-trim case with target θ_0 at an advance ratio of 0.5. Results shown with M_{tip} of 0.183 (left) and 0.549 (right)

small dB increase.

Other configurations such as the wing-trim target C_T case also presented similar increases in tonal noise and broadband noise with three times increased tip speed. This showed that the normal-trim results are representative of the behavior of the other cases. This thought experiment was able to show that the broadband noise is only dominant because of the reduced tip speed of the cases studied, future research with a larger scale model or faster RPM should be a better context to perform a more relevant broadband noise analysis.

Bibliography

[1] Bauknecht A., Wang X., and Chopra I, "Wind Tunnel Test of a Rotorcraft with Lift Compounding," *In 45th European Rotorcraft Forum*, September 2019.

[2] Wang X., Jung Y.S., Baeder J., and Chopra I, "Blade Structural Load/Airload Correlation on a Slowed Mach-Scaled Rotor at High Advance Ratios," *In Journal of the American Helicopter Society*, Vol. 65, (4), 2020, pp. 1-14.

[3] Ananthan S., Baeder J., Sim B.W.C., Hahn S., and Iaccarino G, "Prediction and Validation of the Aerodynamics, Structural Dynamics, and Acoustics of the SMART Rotor Using a Loosely-Coupled CFD-CSD Analysis," *In American Helicopter Society 66th Annual Forum Proceedings*, May 2010.

[4] Shahank M., Wang X., and Chopra I, "Wind Tunnel test on a slowed Mach-Scaled Hingeless Rotor with Lift Compounding," *In Vertical Flight Society 76th Annual Forum Proceedings*, October 2020.

[5] Faust J., Jung Y.S., Baeder J., and Rauleder J, "Aerodynamic Analysis of an Asymmetric Lift-Offset Com-pound Helicopter in Forward Flight using the Mercury CFD Framework," *In Vertical Flight Society technical meeting on Aeromechanics for Advanced Vertical Flight*, January 2020.

[6] Bhar I, "Effect of Interactional Aerodynamics on Computational Aeroacoustics of Sikorsky's Notional X2 Platform," Master of Science in Aerospace Engineering, University of Maryland, 2020.

[7] Ohrle C., Frey F., Thiemeier J., Kebler M., and Kramer E, "Coupled and Trimmed Aerodynamic and Aeroacoustics Simulations for Airbus Helicopters' Compound Helicopter RACER," *In American Helicopter Society technical meeting on Aeromechanics Design for Transformative Vertical Flight*, January 2018.

[8] Jude D., Lee B., Jung Y.S., Petermann J., Govindara-jan B., and Baeder J, "Application of a Heterogeneous CFD Framework Towards Simulating Complete Rotorcraft Configurations," *In American Helicopter Society 74th Annual Forum Proceedings*, May 2018.

[9] Jude D. and Baeder J, "Extending a Three-Dimensional GPU RANS Solver for Unsteady Grid Motion and Free-Wake Coupling," *In 54th AIAA Aerospace Sciences Meeting*, May 2018. San Diego, CA.

[10] Jung Y.S., Govindarajan B, and Baeder J, "Turbulent and Unsteady Flows on Unstructured Line-Based Hamiltonian Paths and Strands Grids," *In AIAA Journal*, Vol. 55,(6), Jun. 2017, pp. 1986-2001.

[11] Medida S. and Baeder J, "Role of Improved Turbulence and Transition Modeling Methods in Rotorcraft Simulations," *In American Helicopter Society 69th Annual Forum*, May 2013.

[12] Spalart P., and Allmaras S., "A One-Equation Turbulence Model for Aerodynamic Flows," *30th AIAA Aerospace Sciences Meeting*, 1992-493, NV, January 1992.

[13] Brazell M. J., Sitaraman J., and Mavriplis D. J., "An overset mesh approach for 3d mixed element high-order discretization," *In Journal of Computational Physics*, Vol. 322, October, 2016, pp. 33-51.

[14] Sridharan A., Rubenstein G., Moy D. M., and Chopra I., "A Python-Based Framework for Computationally Efficient Trim and Real-Time Simulation Using Comprehensive Analysis," *In Journal of the American Helicopter Society*, Vol. 63, (1) , January, 2018, pp. 1-15.

[15] Ananthan S., "Analysis of Rotor Wake Aerodynamics During Maneuvering Flight Using a Free Vortex Wake Methodology," PhD thesis, University of Maryland, College Park, 2006.

[16] Amiraux M, "Numerical Simulation and Validation of Helicopter Blade-Vortex Interaction using Coupled CFD/CSD and Three Levels of Aerodynamic Modeling," Ph. D. dissertation, University of Maryland, College Park, 2014.

[17] Jayasundara D., Jung Y.S., and Baeder J, "CFD andAeroacoustic Analysis of Wingtip-Mounted Propellers," *In Vertical Flight Society 76th Annual Forum Proceedings*, October 2020.

[18] Farassat F. and Succi G.P., "The Prediction of Helicopter Discrete Frequency Noise," *In Vertica*, Vol. 7, (4), 1983, pp. 309-320.

[19] Brooks T., Pope D., and Marcolini M., "Airfoil Self-Noise and Prediction," Tech. rep., RP 1218, NASA, July, 1989.

[20] Jung Y. S., Baeder J., and He C., "Investigation of Empirical Rotor Broadband Prediction using CFD Boundary Layer Parameters Extraction," *Vertical Flight Society's 77th Annual Forum Proceedings*, 2021.